DEPARTMENT OF PHYSICS, UNIVERSITY OF JYVÄSKYLÄ
RESEARCH REPORT No. 2/2000

ELECTRONIC STRUCTURE CALCULATIONS OF ALUMINUM AND SODIUM CLUSTERS

BY
JAAKKO AKOLA

Academic Dissertation
for the Degree of
Doctor of Philosophy

Jyväskylä, Finland
March 2000

URN:ISBN:978-951-39-9465-5
ISBN 978-951-39-9465-5 (PDF)
ISSN 0075-465X

Jyväskylän yliopisto, 2022

ISBN 951-39-0656-6
ISSN 0075-465X

DEPARTMENT OF PHYSICS, UNIVERSITY OF JYVÄSKYLÄ
RESEARCH REPORT No. 2/2000

ELECTRONIC STRUCTURE CALCULATIONS OF ALUMINUM AND SODIUM CLUSTERS

BY
JAAKKO AKOLA

Academic Dissertation
for the Degree of
Doctor of Philosophy

To be presented, by permission of the
Faculty of Mathematics and Natural Sciences
of the University of Jyväskylä,
for public examination in Auditorium FYS 1 of the
University of Jyväskylä on March 31, 2000,
at 12 o'clock noon

Jyväskylä, Finland
March 2000

Preface

The work reviewed in this thesis has been carried out during the years 1997-1999 at the Department of Physics in the University of Jyväskylä.

I would like to thank my supervisors Dr. Hannu Häkkinen and Prof. Matti Manninen for excellent and inspiring guidance during my graduate studies. Working with them has been very effective, educating and pleasant. I am also grateful to Prof. Uzi Landman for his collaboration and hospitality during my several visits to Georgia Tech, and Prof. Lai-Sheng Wang for bringing important experimental aspects into my studies. I also acknowledge useful discussions with Dr. Anniina Rytkönen, Dr. Juha Merikoski, Dr. Stephanie Reimann, Dr. Matti Koskinen and Mr. Stephan Kümmel. Furthermore, I want to thank the Department of Physics for the excellent conditions it has provided for my graduate studies.

The financial support from the Väisälä Foundation, the Nyyssönen Foundation, the Graduate School of Material Physics and the Academy of Finland are gratefully acknowledged. The computational resources for this thesis were provided by the Center for Scientific Computing (CSC).

Finally, I want to thank my beloved wife Stina for her love and support.

Jyväskylä, March 2000

Jaakko Akola

Abstract

This thesis is a review of five publications, where small and medium-sized ($N \leq 102$) aluminum and sodium clusters and their electronic structure are studied using a first-principles simulation method. The initial motivation for these studies was to explain the complicated pattern of measured ionization potentials of small aluminum clusters, which deviates considerably from the corresponding behaviour of alkali clusters. It became evident that in order to explain the experimental results it was necessary to take into account the cluster temperature in the experiments. The effect of the temperature is to lower the ionization potential of the ionic ground state configuration via thermal vibrations of ions and isomerization. The problem was studied using molecular dynamics and so called generalized Koopmans' theorem, which in the density functional regime connects the ionization potential and the energy eigenvalue of the highest occupied single-particle state. Furthermore, the same formalism was applied to the ionization potentials of small sodium clusters, and most convincingly to the photoelectron spectra of aluminum cluster anions. In the case of aluminum cluster anions, the high sensitivity of the electronic spectrum to the geometrical structure allowed a structural assignment of the observed isomers in the experiments.

The main part of this thesis concerns the physical and chemical properties of aluminum clusters. It is observed that the structure of aluminum clusters develops quite rapidly from the icosahedral stacking to the less strained (more or less distorted) decahedral and FCC-lattice based structures. Furthermore, the total shapes of the clusters obey in many instances the so called jellium model, where the positive background density of ions is replaced by a homogeneous charge density. The electronic structure of aluminum clusters evolves rapidly from the strong $s-p$ hybridization to the jellium-like delocalized electronic density, which is perturbed by the crystal field effects caused by the specific geometry of the cluster. Indications of the metallization of aluminum clusters are observed as small energy gaps between the occupied and unoccupied single-particle states, when the cluster size is increased. The binding energies (i.e. the energy required to detach an atom) show a smooth and nearly monotonic increase towards the theoretical bulk value, which within this simulation method was exaggerated. The nearest neighbour distance of aluminum clusters approaches the true bulk value monotonically and rapidly.

List of publications

This thesis consists of an introductory part and of the following publications:

I. Ionization potential of aluminum clusters
J. Akola, H. Häkkinen and M. Manninen,
Phys. Rev. B **58**, 3601 (1998).
https://doi.org/10.1103/PhysRevB.58.3601

II. Ionization potential of Al_6 and Al_7 as a function of temperature
J. Akola, H. Häkkinen and M. Manninen,
Eur. Phys. J. D **9**, 179 (1999).
https://doi.org/10.1007/978-3-642-88188-6_35

III. Temperature-dependent ionization potential of sodium clusters
J. Akola, A. Rytkönen, H. Häkkinen and M. Manninen,
Eur. Phys. J. D **8**, 93 (2000).
https://doi.org/10.1007/s10053-000-9070-z

IV. Photoelectron spectra of aluminum cluster anions: Temperature effects and ab initio simulations
J. Akola, M. Manninen, H. Häkkinen, U. Landman, X. Li and L.-S. Wang,
Phys. Rev. B **60**, 11297 (1999).
https://doi.org/10.1103/PhysRevB.60.R11297

V. Aluminum cluster anions: Photoelectron spectroscopy and ab initio simulations
J. Akola, M. Manninen, H. Häkkinen, U. Landman, X. Li and L.-S. Wang,
manuscript under construction.
https://doi.org/10.1103/PhysRevB.62.13216

The author has written publications II and III. Publication I was written by Dr. Hannu Häkkinen and publications IV and V were written in co-operation with the author, Dr. Hannu Häkkinen and Prof. Uzi Landman. The author has performed most of the numerical work and interpretation of the results in all the publications. The experimental results presented in publications IV and V are measured by Mr. Xi Li and Prof. Lai-Sheng Wang.

Contents

1 Introduction **3**

2 Theoretical background **7**
2.1 Many-body Schrödinger equation 7
2.2 Pseudopotentials 14
2.3 Jellium model 16

3 Density functional theory **19**
3.1 Kohn-Sham method 19
3.2 Local density approximation 23
3.3 Physical interpretation of the KS energy eigenvalues 26
3.4 BO-LSD-MD method 28

4 Main results **33**
4.1 Small aluminum clusters 33
4.2 Temperature effects on ionization potential of clusters 39
4.3 Photoelectron spectroscopy of aluminum cluster anions 44
4.4 Larger aluminum cluster anions 51

5 Summary **59**

Chapter 1

Introduction

Atomic clusters are aggregates composed of a countable number of atoms, starting from a two atom dimer and reaching an indefinite upper limit of several hundred thousand atoms. Therefore, they describe the vast transition from a single atom to the bulk material. Clusters differ from conventional molecules because of their composition and structure [1]. Usually, molecules have a definite number of atoms and specific compositions. In many instances molecules also have unique structures. Clusters however may be composed of any number N of component particles, and, as the number of composite particles increases, the number of locally stable structures (isomers) grows rapidly. Furthermore, clusters differ from the bulk material because of their finite size. As a consequence, a large fraction of the constituent atoms is located on the surface of the cluster (e.g. for a spherical cluster of 1000 atoms about 40%). In addition, the electronic band structure of solids does not exist for clusters, where the electronic energy spectrum consists of discrete levels because of the finite number of electrons. The small dimension of clusters leads to some properties characterized by the quantum effects, whereas in the macroscopic domain the same properties can be described classically.

Although the first practical applications of metal clusters were invented already by the glaziers of Middle Ages [2], the most fascinating features, which started the modern cluster research, were not observed until 1980s. Up to this point much of the cluster research was concentrated on the electromag-

netic properties of glasses and related systems. Even during 60's and 70's, there was little reason to expect common patterns for clusters with different sizes and elements. Therefore, the small clusters were considered as small unique molecules, which could be treated via quantum-chemical methods, and the larger clusters in the mesoscopic domain were described using the approaches of solid state physics and statistical mechanics.

Situation changed drastically in 1983, when the electronic shell structure of small sodium clusters ($N < 100$) was experimentally observed from the mass abundance spectrum [3]. The most abundant cluster sizes (i.e. shell closings) were observed to match with the predictions of a simple square well potential calculated using a spherical jellium model, where the ionic background density was smoothed [4]. After this discovery the development was fast. Experimentally, the electronic shell structure was observed for many simple and noble metal clusters, and it was further verified in the electronic response properties (such as ionization potential, polarizability, plasmons, etc.) of metallic clusters [2]. Theoretically, the jellium model was further developed and successfully applied to metal clusters in conjunction with the experiments [5]. The sudden increase in the cluster research gave also its own motivation to improve the quantum-chemical *ab initio* methods, which at this point were mainly used for conventional molecules [6, 7, 8, 9].

The physical and chemical properties of clusters approach to the bulk values as the number of composite atoms increases. This is an important motivation for the cluster research since by studying these finite systems one can also learn how the properties of infinite bulk systems emerge from the properties of clusters, as the clusters grow larger and larger. Furthermore, one can learn about the different size-evolutionary patterns of different materials. For example, properties like cluster geometries, thermodynamic stability, abundance distributions, electronic and vibrational spectra, dissociation and ionization energies, and chemical reactivity, may exhibit different size-evolutionary trends for different materials as the cluster size is varied. Naturally, this leads finally to the well-known properties of bulk matter. In addition, clusters may be used for designing new kinds of cluster based materials (such as based on C_{60}), for developing chemical reactions in new ways (surface catalysis), and hopefully in the near future for manufacturing technological applications (embedded clusters).

As an example of the above-mentioned size-evolutionary patterns, both theo-

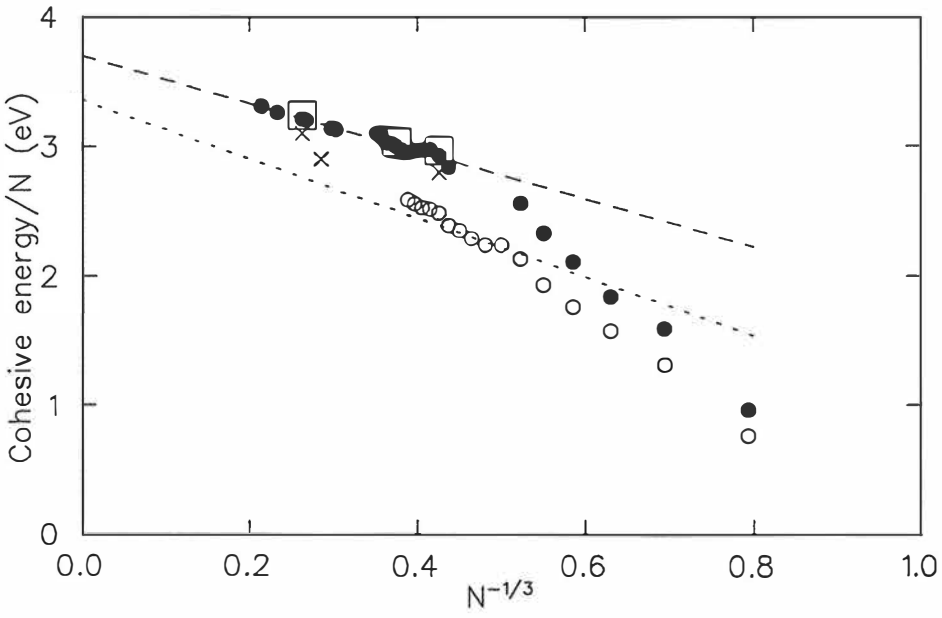

Figure 1.1: Cohesive energies per atom (in eV). Open circles: photodissociation experiment (Ref. [10]), solid dots: BO-LSD-MD results (this thesis), open squares: Car-Parrinello calculations (Ref. [11]), and crosses: DVM $X\alpha$ results (Ref. [12]).

retical and experimental cohesive energies of aluminum clusters are presented in Fig. 1.1. In order to demonstrate the special dependence between the cohesive energy E_C and the atom number N, E_C is presented as a function of $N^{-1/3}$. It is evident, that the cohesive energy achieves quite rapidly a linear behaviour with this choice of variables. The dashed line corresponding to the theoretical results is fitted to the E_C value of larger clusters ($N \geq 12$), and its extrapolation to the E_C-axis gives the theoretical prediction 3.70 eV for the bulk cohesive energy. Similar linear fit is also used for the experimental values, which is fixed into the real bulk cohesive energy 3.36 eV. The clear systematic error in the theoretical results is expected and due to the calculational details (local density approximation, Chap. 3).

The main emphasis in this thesis is on a theoretical description of aluminum clusters via a first-principles simulation method called the Born-Oppenheimer local-spin-density molecular dynamics (BO-LSD-MD) method [13]. As it is well-known, aluminum is a simple metal, and it differs considerably in a small size regime from the alkalis because of its three valence electrons (two $3s$ and one $3p$). Indeed, the initial motivation of this thesis was to study

the interesting features of small aluminum clusters ($N \leq 20$) observed in the experimental ionization potentials [14, 15] and mass abundance spectrum [16, 17, 18], which deviated considerably from the corresponding results measured for small alkali clusters [3, 18, 19]. A number of similar theoretical studies mainly concentrating to the size range $N \leq 10$ had already been published [20, 21, 22, 23], and some efforts to explore also the larger aluminum clusters were made [11, 12, 23]. However, during this study it became evident, that one had to take also the experimental conditions (mainly the temperature of produced clusters) into account in order to obtain consistent results, and therefore it was necessary to use a temperature-dependent theoretical model for further investigations. In addition, the physical meaning of the calculational single-electron states (so called Kohn-Sham states) [24] is employed in the description of photoionization efficiency curves of small aluminum and sodium clusters, and photoelectron spectra of aluminum cluster anions. In these studies, further information about the structural and electronic properties of aluminum and sodium clusters is obtained. Especially in the case of aluminum, a profound understanding of the physical and chemical properties of small and medium-sized aluminum clusters ($N \leq 102$) is achieved.

The outline of this thesis is the following: In Chapter 2 the basic theoretical concepts and related approximations concerning many-body calculations on finite fermion systems are briefly discussed. The theoretical considerations are further continued in Chap. 3, where the density functional theory and its Kohn-Sham formulation are presented together with a detailed description of the BO-LSD-MD method used throughout this thesis. The main results concerning the physical and chemical properties of aluminum clusters, the temperature-dependent ionization potentials of aluminum and sodium clusters, and the determination of the temperature-dependent photoelectron spectra of aluminum cluster anions are displayed in Chap. 4. The concluding remarks appear in Chap. 5.

Chapter 2

Theoretical background

2.1 Many-body Schrödinger equation

The basic problem considered in this thesis is to find an approximate solution to the time-independent many-body Schrödinger equation

$$H|\Phi\rangle = E|\Phi\rangle, \tag{2.1}$$

where H is a Hamiltonian for a system of nuclei and electrons described by position vectors $\{\mathbf{R}_A\}$ and $\{\mathbf{r}_i\}$, respectively. The corresponding non-relativistic many-body Hamiltonian [25] (where N and M are the number of electrons and nuclei, respectively) can be written in atomic units[1] (used throughout this thesis) as

$$\begin{aligned} H = &-\sum_{i=1}^{N} \frac{1}{2}\nabla_i^2 - \sum_{A=1}^{M} \frac{1}{2M_A}\nabla_A^2 - \sum_{i=1}^{N}\sum_{A=1}^{M} \frac{Z_A}{r_{iA}} \\ &+ \sum_{i=1}^{N}\sum_{j>i}^{N} \frac{1}{r_{ij}} + \sum_{A=1}^{M}\sum_{B>A}^{M} \frac{Z_A Z_B}{R_{AB}}. \end{aligned} \tag{2.2}$$

In this equation, M_A is the ratio of the mass of nucleus A to the mass of an electron, and Z_A is the atomic number of nucleus A. The differential

[1] The atomic units of energy and length are Hartree (=27.21 eV) and Bohr (=0.529 Å), respectively.

operators ∇_i^2 and ∇_A^2 involve differentiation with respect to the coordinates of ith electron and Ath nucleus. The first and second term of Eq. (2.2) are the kinetic energy operators for the electrons and nuclei, respectively; the third term represents the Coulomb attraction between electrons and nuclei; the fourth and fifth terms correspond to the Coulomb repulsion between electrons and between nuclei, respectively.

From a calculational point of view, the many-body Hamiltonian in Eq. (2.2) has an undesirable property: it contains both electronic and nucleonic parts. However, this problem can be easily overcome by introducing an adiabatic approximation called the Born-Oppenheimer (BO) approximation [26, 27, 28]. In this approximation the wave function is separated into two independent parts

$$|\Phi\rangle = |\Phi_{elec}\rangle \cdot |\Phi_{nucl}\rangle \tag{2.3}$$

describing the solutions of electrons and nuclei, respectively. The physical justification for the use of this approximation is the dramatically different time scales of electrons and nuclei, since nuclei as heavier particles move much more slowly than electrons. Therefore, one can consider that for each nuclear configuration the electronic part of the total wave function is in its ground state. The resulting electronic Schrödinger equation is then

$$H_{elec}|\Phi_{elec}\rangle = E_{elec}|\Phi_{elec}\rangle, \tag{2.4}$$

where the electronic Hamiltonian

$$H_{elec} = -\sum_{i=1}^{N} \frac{1}{2}\nabla_i^2 - \sum_{i=1}^{N}\sum_{A=1}^{M} \frac{Z_A}{r_{iA}} + \sum_{i=1}^{N}\sum_{j>i}^{N} \frac{1}{r_{ij}} \tag{2.5}$$

describes the motion of N electrons in the field of M fixed point charges. The solution of Eq. (2.4) yields an electronic wave function

$$|\Phi_{elec}\rangle = |\Phi_{elec}(\{\mathbf{r}_i\};\{\mathbf{R}_A\})\rangle, \tag{2.6}$$

which depends explicitly on the electronic coordinates and parametrically on the nuclear coordinates. Also the electronic energy

$$E_{elec} = E_{elec}(\{\mathbf{R}_A\}) \tag{2.7}$$

has a parametric dependence of the nuclear coordinates. According to these findings, one can now observe that the altering of the nuclear configuration yields different solutions for $|\Phi_{elec}\rangle$ and E_{elec}. Furthermore, the inclusion of

the nuclear repulsion (last term in Eq. (2.2)) allows one to write the total energy of the fixed system as

$$E_{tot} = E_{elec} + \sum_{A=1}^{M} \sum_{B>A}^{M} \frac{Z_A Z_B}{R_{AB}}. \tag{2.8}$$

The equations (2.4) and (2.8) constitute now the electronic problem.

After solving the electronic problem it is possible to introduce the nuclear problem

$$H_{nucl}|\Phi_{nucl}\rangle = E|\Phi_{nucl}\rangle, \tag{2.9}$$

where the nuclear Hamiltonian is according to the Born-Oppenheimer approximation

$$H_{nucl} = -\sum_{A=1}^{M} \frac{1}{2M_A}\nabla_A^2 + E_{tot}(\{\mathbf{R}_A\}). \tag{2.10}$$

The nuclear wave function

$$|\Phi_{nucl}\rangle = |\Phi_{nucl}(\{\mathbf{R}_A\})\rangle \tag{2.11}$$

describes now the vibration, rotation and translation of the system, and the total energy E in Eq. (2.9) takes these contributions into account.

Furthermore, concerning the motion of ions, an important result is obtained when the electronic energy of the system $E_{elec} = \langle\Phi_{elec}|H_{elec}|\Phi_{elec}\rangle$ is differentiated with respect to some ionic coordinate $R_{A,\gamma}$ (in the cartesian coordinates $\gamma = x, y, z$)

$$\begin{aligned} \frac{\partial E_{elec}(\{\mathbf{R}_A\})}{\partial R_{A,\gamma}} &= \left\langle \Phi_{elec} \middle| \frac{\partial H_{elec}}{\partial R_{A,\gamma}} \middle| \Phi_{elec} \right\rangle \\ &= \left\langle \Phi_{elec} \middle| \frac{\partial V(\{\mathbf{r}_i\};\{\mathbf{R}_A\})}{\partial R_{A,\gamma}} \middle| \Phi_{elec} \right\rangle, \end{aligned} \tag{2.12}$$

where

$$V(\{\mathbf{r}_i\};\{\mathbf{R}_A\}) = -\sum_{i=1}^{N} \sum_{A=1}^{M} \frac{Z_A}{r_{iA}} \tag{2.13}$$

is the classical potential acting between electrons and nuclei. Above the fact, that the kinetic energy and Coulomb repulsion of electrons in Eq. (2.5) do not depend on the coordinates $\{\mathbf{R}_A\}$, has been employed. The resulting Eq. (2.12) is the famous Hellmann-Feynman theorem [29], and its significance is

that within the BO approximation the forces acting on nuclei are derivable from the classical potential (2.13) and the electronic wave function $|\Phi_{elec}\rangle$. Thus, if the force component $F_{A,\gamma}$ acting on a nuclei A is written as

$$F_{A,\gamma} = -\frac{\partial E_{elec}(\{\mathbf{R}_A\})}{\partial R_{A,\gamma}} \tag{2.14}$$

it is seen that $F_{A,\gamma}$ is achieved from the derivative of classical potential averaged over the electronic wave function (density). Combining the resulting forces $\{\mathbf{F}_A\}$ with the Coulomb repulsion of nuclei gives now the classical total forces acting on ions.

The main difficulty of the many-body Schrödinger equation (2.1) arises in the determination of the electronic solution $|\Phi_{elec}\rangle$. Therefore, we concentrate in the rest of the chapter solely to the electronic problem (2.4). The most convenient approach to this many-body problem is the variational principle, which states that when the system is described by the state $|\Psi\rangle$ the average energy of many measurements is given by the formula

$$E[\Psi] = \frac{\langle\Psi|H|\Psi\rangle}{\langle\Psi|\Psi\rangle}. \tag{2.15}$$

It is worthwhile to mention that the wave function $|\Psi\rangle$ does not have to satisfy the initial Schrödinger equation. Since each particular measurement of the energy gives one of the eigenvalues of H, we immediately have

$$E[\Psi] \geq E_0, \tag{2.16}$$

where E_0 is the true ground state energy of the system. As a result, the full minimization of the functional $E[\Psi]$ with respect to all allowed N-electron wave functions leads to the true ground state $|\Psi_0\rangle$ and energy $E[\Psi_0] = E_0$. In practice, the variational method requires a trial wave function, and the parameters of this trial function are optimized in order to minimize the energy $E[\Psi]$. It is important to emphasize that the constraints of the trial function determine how close one can get to the real ground state energy E_0.

Let us next consider an N-electron trial wave function corresponding to the case of noninteracting electrons described by the Hamiltonian

$$H = \sum_{i=1}^{N} h(i), \tag{2.17}$$

where the single-particle operator $h(i)$ operates to the single-particle spin orbital $|\psi_j(\mathbf{x}_i)\rangle$ (notation $\mathbf{x}_i$ contains both the position and the spin of ith electron). The corresponding many-body wave function is a direct product

$$|\Psi^{HP}(\mathbf{x}_1, \mathbf{x}_2, ..., \mathbf{x}_N)\rangle = |\psi_i(\mathbf{x}_1)\psi_j(\mathbf{x}_2)...\psi_k(\mathbf{x}_N)\rangle. \tag{2.18}$$

This kind of a many-electron wave function is called the Hartree product, and it has one important deficiency: it does not fulfill the antisymmetry principle of fermions i.e. the wave function does not change its sign when two spin orbitals (electrons) are interchanged. Consequently, the minimization of energy using this trial function does not lead to the true ground state energy and wave function.

The antisymmetry requirement is taken into account in the Hartree-Fock (HF) theory, where the normalized many-electron wave function is a Slater determinant

$$\begin{aligned} |\Psi^{HF}(\mathbf{x}_1, \mathbf{x}_2, ..., \mathbf{x}_N)\rangle &= \frac{1}{\sqrt{N!}} \begin{vmatrix} |\psi_i(\mathbf{x}_1)\rangle & |\psi_j(\mathbf{x}_1)\rangle & \dots & |\psi_k(\mathbf{x}_1)\rangle \\ |\psi_i(\mathbf{x}_2)\rangle & |\psi_j(\mathbf{x}_2)\rangle & \dots & |\psi_k(\mathbf{x}_2)\rangle \\ \vdots & \vdots & \ddots & \vdots \\ |\psi_i(\mathbf{x}_N)\rangle & |\psi_j(\mathbf{x}_N)\rangle & \dots & |\psi_k(\mathbf{x}_N)\rangle \end{vmatrix} \\ &= \frac{1}{\sqrt{N!}} \det[\psi_i, \psi_j, ..., \psi_k] \end{aligned} \tag{2.19}$$

consisting of single-particle spin orbitals $|\psi(\mathbf{x}_i)\rangle$. At this point one should notice that although the wave function is now much more complicated than the initial Hartree product the single-particle picture is still maintained. The consequent energy expectation value is

$$E^{HF} = \langle \Psi^{HF}|H|\Psi^{HF}\rangle = \sum_{i=1}^{N} H_i + \frac{1}{2}\sum_{i,j=1}^{N}(J_{ij} - K_{ij}), \tag{2.20}$$

where

$$H_i = \int \psi_i^*(\mathbf{x})\Big[-\frac{1}{2}\nabla^2 + v(\mathbf{x})\Big]\psi_i(\mathbf{x})d\mathbf{x}, \tag{2.21}$$

$$J_{ij} = \int\int \psi_i(\mathbf{x}_1)\psi_i^*(\mathbf{x}_1)\frac{1}{r_{12}}\psi_j^*(\mathbf{x}_2)\psi_j(\mathbf{x}_2)d\mathbf{x}_1 d\mathbf{x}_2, \tag{2.22}$$

$$K_{ij} = \int\int \psi_i^*(\mathbf{x}_1)\psi_j(\mathbf{x}_1)\frac{1}{r_{12}}\psi_i(\mathbf{x}_2)\psi_j^*(\mathbf{x}_2)d\mathbf{x}_1 d\mathbf{x}_2. \tag{2.23}$$

These integrals are all real, and $J_{ij} \geq K_{ij} \geq 0$. The J_{ij} are called Coulomb integrals and they describe the classical repulsion of electrons. The K_{ij} are

called exchange integrals and they are quantum mechanical energy contributions caused by the antisymmetrization of the wave function.

By minimizing E^{HF} with respect to the choice of spin orbitals and normalization constraint

$$\int \psi_i^*(\mathbf{x})\psi_j(\mathbf{x})d\mathbf{x} = \delta_{ij}, \tag{2.24}$$

one can derive an equation called the Hartree-Fock equation, which determines the optimal spin orbitals. The form of this eigenvalue equation is

$$f(i)|\psi(\mathbf{x}_i)\rangle = \epsilon|\psi(\mathbf{x}_i)\rangle, \tag{2.25}$$

where $f(i)$ is an effective one-electron operator

$$f(i) = -\frac{1}{2}\nabla_i^2 - \sum_{A=1}^{M}\frac{Z_A}{r_{iA}} + v^{HF}(i), \tag{2.26}$$

called the Fock operator. The operator v^{HF} could be regarded as the average potential (although it is not really a potential) experienced by the ith electron due to the presence of the other electrons. The Hartree-Fock equation (2.25) is a nonlinear equation since the operator v^{HF} depends on the spin orbitals of other electrons. Therefore, it has to be solved iteratively. In practice, this is performed by guessing the initial spin orbitals and calculating the corresponding average potential v^{HF}. After that one is able to solve the eigenvalue equation for a new set of spin orbitals. Using these orbitals it is possible to calculate the new average potential and repeat the procedure until the self-consistency is achieved.

Although the Hartree-Fock theory includes the antisymmetry requirement, it is still not complete. This is a consequence of the single-determinantal description of the many-body wave function causing the minimized energy to deviate from the true ground state energy E by amount

$$E_{corr}^{HF} = E - E^{HF}. \tag{2.27}$$

This difference is called the correlation energy (defined here to be negative) and its reliable determination is a major problem in many-body theories.

The correlation energy can be taken into account by expanding the HF single-determinant wave function to the multi-determinantal form

$$|\Phi\rangle = c_0|\Psi_0\rangle + \sum_{r,a} c_a^r|\Psi_a^r\rangle + \sum_{\substack{a<b\\r<s}} c_{ab}^{rs}|\Psi_{ab}^{rs}\rangle + \sum_{\substack{a<b<c\\r<s<t}} c_{abc}^{rst}|\Psi_{abc}^{rst}\rangle + \ldots \tag{2.28}$$

where $|\Psi_0\rangle$ is the Hartree-Fock ground state and the following determinants correspond to the excited states, where an electron from the state a has been excited to the virtual state r, and so on. In order to get the true ground state energy one has to calculate the HF determinants $|\Psi_i\rangle$ and minimize the energy with respect to the coefficient c_0, c_a^r, c_{ab}^{rs},... and the normalization constraint $\langle\Phi|\Phi\rangle = 1$. This procedure is called the configuration interaction (CI) method since each $|\Psi_i\rangle$ can be defined by specifying a configuration of spin orbitals from which it is formed. In practice, it is impossible to include an infinite number of different excited determinants into CI calculations, and therefore only a certain (usually small) number of excited states are considered.

The determinantal many-body wave function methods described above are calculationally very expensive. Consequently, the methods are applicable only to the smallest clusters and molecules. This restriction can however be avoided by introducing a totally new perspective to the electronic structure calculations called the density functional theory (DFT) [7, 8, 30]. In this method one abandons the many-body wave function and concentrates instead on the electron density

$$\rho(\mathbf{x}_1) = N \int \int ... \int |\Psi(\mathbf{x}_1, \mathbf{x}_2, ..., \mathbf{x}_N)|^2 ds_1 d\mathbf{x}_2 ... d\mathbf{x}_N, \tag{2.29}$$

where ds_1 corresponds to the integration with respect to the spin of particle 1 and N is the total number of electrons according to equation

$$N = \int \rho(\mathbf{r}) d\mathbf{r}. \tag{2.30}$$

The first Hohenberg-Kohn [8, 31] theorem states that all the properties of the nondegenerate many-body ground state can be calculated from the electron density. The proof of this, which is not presented here, is simple and relies on the variational principle[2]. As a result, the energy can now be presented as a functional of electron density $\rho(\mathbf{r})$ as

$$E[\rho] = T[\rho] + V_{ne}[\rho] + V_{ee}[\rho], \tag{2.31}$$

where $T[\rho]$ is the kinetic energy functional, $V_{ne}[\rho]$ is the energy functional corresponding to the interaction between nuclei (external potential) and electrons, and $V_{ee}[\rho]$ is the electron-electron energy functional. Furthermore, the

[2]Levy [32] has offered a more general proof for this theorem, which shows that it applies also for degenerate ground states.

second Hohenberg-Kohn theorem [8, 31] states that for a random trial density $\tilde{\rho}(\mathbf{r})$, which obeys the conditions $\tilde{\rho}(\mathbf{r}) \geq 0$ and $\int \tilde{\rho}(\mathbf{r})d\mathbf{r} = N$, applies

$$E_0 \leq E[\tilde{\rho}], \tag{2.32}$$

where $E[\tilde{\rho}]$ is a functional corresponding to Eq. (2.31). This theorem allows us now to use the variational principle for the determination of the ground state energy and electron density via the variational equation

$$\delta\Big\{E[\rho] - \mu\Big[\int \rho(\mathbf{r})d\mathbf{r} - N\Big]\Big\} = 0, \tag{2.33}$$

where μ is a Lagrange undetermined multiplier. Furthermore, by requiring that the above equation applies to an arbitrary density variation $\delta\rho(\mathbf{r})$ one is lead to the Euler-Lagrange equation

$$\mu = \frac{\delta E[\rho]}{\delta\rho(\mathbf{r})}, \tag{2.34}$$

where the physical meaning of quantity μ is the chemical potential. If the functional $E[\rho]$ is known, it is possible to calculate the electron density $\rho(\mathbf{r})$ using Eq. (2.34). The density functional theory and its Kohn-Sham [8, 33] formulation are further studied in the next chapter.

2.2 Pseudopotentials

The theoretical approach has so far considered all the electrons and nuclei of the system explicitly. In practice, this is however very time consuming even in the density functional regime, and alternative methods have to be developed in order to model also larger systems ($N_e \geq 100$). In the pseudopotential approximation [34] the atom is separated to valence electrons and an ionic core. The ionic core is described by an average potential (pseudopotential) of nucleus and core electrons, where the effects of core electrons (screening and the Pauli exclusion principle) are taken into account. The idea here is to explicitly describe the valence electrons, which determine the physical properties of the atom, as interacting particles in the field created by the ionic cores. This kind of an assumption generally works very well and it has been successfully employed in the atomic and molecular physics.

There is a large number of different pseudopotentials developed for various purposes. The most advanced ones, which are made for quantum-chemical *ab initio* calculations, are nonlocal and free of adjustable parameters, but also difficult to use for complex molecules and clusters. At short distances from the nucleus, these pseudopotentials are usually repulsive due to the Pauli exclusion principle, and at large distance they fall off asymptotically as the coulombic potential of the unscreened effective charge of the ion. Interestingly, the pseudopotentials of simple metals like the alkalis are rather weak explaining the success of jellium model (discussed in the next section) for these metals [5].

One of the simplest possible pseudopotentials obeying the main requirements discussed above is the Ashcroft's pseudopotential [35]. It is a coulombic potential, which is cut off at so-called empty core radius r_c, and is set equal to zero inside

$$\begin{aligned} V_{ps}(r) &= -\frac{Z}{r}, \quad \text{for} \quad r \geq r_c \\ &= 0, \quad \text{for} \quad r < r_c. \end{aligned} \tag{2.35}$$

This pseudopotential has been successfully applied to bulk and surface properties of solids [26]. Another very simple pseudopotential has been developed by Manninen [36], where

$$\begin{aligned} V_{ps}(r) &= -\frac{Z}{r}, \quad \text{for} \quad r \geq r_c \\ &= -\frac{3Z}{2r_c^3}\left[r_c^2 - \frac{r^2}{3}\right], \quad \text{for} \quad r < r_c. \end{aligned} \tag{2.36}$$

This potential is actually the electrostatic potential of a homogeneously charged sphere of radius r_c, and it was applied by Manninen to small alkali clusters.

The modern pseudopotentials are much more sophisticated than the ones presented above. In addition to the several new physical requirements (such as angular momentum dependence, norm-conservation, nonlocality, separability, etc.) one has to consider also calculational effectiveness of a certain kind of pseudopotential for a given basis set[3]. For instance, Troullier and Martins [37] have shown for a plane wave basis that the fastest convergence of total energy is achieved using very smooth pseudopotentials.

[3]The calculational effectiveness is here related to the rate of convergence of the total energy when the basis set is expanded.

2.3 Jellium model

In the pseudopotential approximation the valence electrons are separated from the rest of the atom, and the resulting ion is described by an effective pseudopotential. In order to make calculations easier, the pseudopotential treatment is next further simplified by completely ignoring the resulting ionic structure, and replacing it by a homogeneous background density in a finite volume. This approximation is called the jellium model, and it was first applied to metallic bulk and surface properties by Lang and Kohn [38]. The quantum mechanical self-consistent field of electrons can be calculated using this model. For this purpose, the charge density of the ionic background (so-called Wigner-Seitz radius r_s) has to be specified as an external parameter, which characterizes the properties of the metal.

At first glance, one might think that the total neglect of ionic structure in the jellium approximation is too drastic an assumption. In fact, this is true for most of the ordinary molecules. However, in the case of metal clusters and metals, the jellium picture is justified because of the delocalized valence electrons, which experience a weak and smoothly changing net pseudopotential caused by the ion cores. Therefore, the further smoothing of the ionic background does not introduce any significant qualitative changes to the physical picture.

There are many ways to do jellium calculations. Above, the discussion has considered the self-consistent treatment of the valence electrons. [4, 39, 40, 41]. Furthermore, many studies have been made using a phenomenological jellium model [42, 43, 44, 45], where the iterative calculation of the self-consistent field of valence electrons is avoided by including it to some easy-to-use average single-particle potential. The resulting problem is now much easier since the Schrödinger equation has to be solved only once.

One of most popular choices for the phenomenological single-particle potential is the spherical Woods-Saxon potential

$$V(r) = -\frac{V_0}{1 + e^{\alpha(r-r_0)}}, \tag{2.37}$$

where V_0 and r_0 are the depth and radius of the potential well, respectively. The parameter α determines the potential softness at the surface of the clus-

ter. For physical reasons, the Woods-Saxon potential has usually a steep rise at the surface causing the potential resemble closely to the simple square well. Consequently, the electronic eigenvalue spectra of these two potential are similar. The corresponding electronic shells according to the three-dimensional square well (the analytically solvable eigenstates are Bessel functions) are in order $1s$, $1p$, $1d$, $2s$, $1f$, $2p$, $1g$, $2d$, $1h$, $3s$,... and the electron numbers of the shell closings (so-called magic numbers) are 2, 8, 18, 20, 34, 40, 58, 68, 90, 92,... The numbers 18 and 90 are underlined because the corresponding electron shell is usually nearly degenerate with the higher electron shell.

The geometry of the cluster is determined in the jellium model by the shape of the background density. The simplest case is the spherical jellium model, where the Schrödinger equation reduces into a one-dimensional equation due to the spherical symmetry. This problem can be easily solved even for large clusters. Usually, the equilibrium shapes are spherical for the jellium clusters corresponding to the above shell closings. These clusters also have a high relative stability according to the total energy (i.e. they are magic). The situation complicates for the open shell clusters, because the shape of the cluster deforms due to the Jahn-Teller effect [46], which tends to break the degeneracy of the occupied and unoccupied states by reducing the symmetry of the system. The simplest deformed cluster shapes are prolate and oblate, which correspond to quadrupole deformations. Furthermore, one can consider also higher-order deformations such as octupole and hexadecupole deformations.

In practice, the jellium model has been studied extensively for finite metal clusters [5]. Both self-consistent and phenomenological approaches have been successfully employed in order to explain the experimentally observed properties of metal clusters, in particular those of alkali clusters [2]. Deformations of the jellium background and the finite temperature of the electron density can be taken into account at reasonable cost [47, 48]. In this thesis, the jellium model is used only as a reference system for aluminum clusters. Although aluminum is a simple metal, it differs remarkably from alkalis because of its much stronger pseudopotentials. Therefore, one cannot expect a similar correspondence to the jellium model as it is shown in many instances [2].

Chapter 3

Density functional theory

3.1 Kohn-Sham method

In this section the Kohn-Sham (KS) method [8, 33] is discussed. The method was developed in order to describe atoms and molecules more accurately than the conventional Thomas-Fermi-Dirac (TFD) method, which was based on a direct approach to the variational problem. This was necessary since the TFD model was observed to fail to produce the shell structure of atoms and even the further modifications of this method were not successful [30].

Let us first consider noninteracting electrons. The corresponding Hamiltonian is (the electron spin is neglected at the moment)

$$H_s = \sum_{i=1}^{N} \Big[-\frac{1}{2}\nabla_i^2 + v_s(\mathbf{r}_i) \Big], \tag{3.1}$$

where the external potential $v_s(\mathbf{r}_i)$ is in the case of atomic clusters and molecules the coulombic potential of ions. As was earlier mentioned in the context of Hartree products (Sec. 2.1.), the solution of the Schrödinger equation $H_s|\Psi_s\rangle = E_s|\Psi_s\rangle$ can be written as a product of single-particle wave functions

$$|\Psi_s(\mathbf{r}_1, \mathbf{r}_2, ..., \mathbf{r}_N)\rangle = |\psi_1(\mathbf{r}_1)\rangle|\psi_2(\mathbf{r}_2)\rangle \cdots |\psi_N(\mathbf{r}_N)\rangle, \tag{3.2}$$

which themselves are solutions to the single-particle Schrödinger equation

$$\Big[-\frac{1}{2}\nabla_i^2 + v_s(\mathbf{r}_i)\Big]\psi_i(\mathbf{r}) = \epsilon_i\psi_i(\mathbf{r}). \tag{3.3}$$

Furthermore, by taking into account the antisymmetry requirement of fermions, one can conclude that the exact solution of the noninteracting system is a Slater determinant, which consists of the aforementioned single-particle wave functions. Therefore, the exact electron density is

$$\rho(\mathbf{r}) = \sum_{i=1}^{N} |\psi_i(\mathbf{r})|^2, \tag{3.4}$$

where the sum goes over N energetically lowest single-particle states (electrons). In order to achieve this particularly simple result, one needs to solve only the single-particle Schrödinger equation (3.3).

The idea of Kohn and Sham was to use in the case of interacting electrons the kinetic energy functional

$$T_s[\rho] = \sum_{i=1}^{N}\langle\psi_i| - \frac{1}{2}\nabla^2|\psi_i\rangle, \tag{3.5}$$

which is exactly defined for the noninteracting electrons. Of course, this is not the correct kinetic energy functional, but in the KS formulation T_s is treated as a true kinetic energy. It has been confirmed by calculations that this is in fact a reasonably good approximation. Furthermore, the missing part of the true T is usually taken into account in another energy functional called the exchange-correlation energy E_{xc}. The energy functional according to the KS method is now

$$E[\rho] = T_s[\rho] + V_{ne}[\rho] + J[\rho] + E_{xc}[\rho], \tag{3.6}$$

where

$$V_{ne}[\rho] = \int v(\mathbf{r})\rho(\mathbf{r})d\mathbf{r} \tag{3.7}$$

and

$$J[\rho] = \frac{1}{2}\int\int \frac{\rho(\mathbf{r}_1)\rho(\mathbf{r}_2)}{r_{12}} d\mathbf{r}_1 d\mathbf{r}_2 \tag{3.8}$$

are the energy functionals corresponding to the interaction between electrons and external potential, and the coulombic electron-electron repulsion, respectively. The exact exchange-correlation potential E_{xc} containing the quantum

mechanical electron-electron interaction terms is not exactly known, and it is further discussed in the next section.

Using Eq. (3.6), the Euler-Lagrange equation has now the form

$$\mu = \frac{\delta E[\rho]}{\delta \rho(\mathbf{r})} = v_{eff}(\mathbf{r}) + \frac{\delta T_s[\rho]}{\delta \rho(\mathbf{r})}, \tag{3.9}$$

where the effective KS potential is defined as follows

$$\begin{aligned} v_{eff}(\mathbf{r}) &= v(\mathbf{r}) + \frac{\delta J[\rho]}{\delta \rho(\mathbf{r})} + \frac{\delta E_{xc}[\rho]}{\delta \rho(\mathbf{r})} \\ &= v(\mathbf{r}) + \int \frac{\rho(\mathbf{r}')}{|\mathbf{r} - \mathbf{r}'|} d\mathbf{r}' + v_{xc}(\mathbf{r}) \end{aligned} \tag{3.10}$$

and the exchange-correlation potential is

$$v_{xc}(\mathbf{r}) = \frac{\delta E_{xc}[\rho]}{\delta \rho(\mathbf{r})}. \tag{3.11}$$

The KS effective potential v_{eff} in Eq. (3.10) has clearly a similar role than the plain external potential v_s in the noninteracting case. Therefore, it is straightforward to replace the interactionless single-particle Schrödinger equation by a similar equation

$$\Big[-\frac{1}{2}\nabla^2 + v_{eff}(\mathbf{r}) \Big] \psi_i(\mathbf{r}) = \epsilon_i \psi_i(\mathbf{r}) \tag{3.12}$$

corresponding to interacting electrons. Furthermore, the electron density, which satisfies Eq. (3.9), is obtained from equation

$$\rho(\mathbf{r}) = \sum_{i=1}^{N} |\psi_i(\mathbf{r})|^2. \tag{3.13}$$

Since v_{eff} itself depends on the density $\rho(\mathbf{r})$, one must solve equations (3.10)-(3.13) self-consistently. These equations are called the Kohn-Sham equations. In practice, the calculations are started from a trial density $\rho(\mathbf{r})$, which is used to determine the effective potential v_{eff} in Eq. (3.10). After this, a new density $\rho(\mathbf{r})$ is obtained from the equations (3.12) and (3.13). The procedure is repeated until the self-consistency is achieved, and the resulting total energy can be calculated from Eq. (3.6).

So far, the spin of the electron has been neglected. However, in the presence of an external magnetic field or for an odd number of electrons, the KS

method has to be extended to include spin-dependency. Instead of the electron density $\rho(\mathbf{r})$, the basic variables are now the α-electron density $\rho^\alpha(\mathbf{r})$ and the β-electron density $\rho^\beta(\mathbf{r})$ (where α and β denote different directions of the electron spin) or alternatively the electron spin density $Q(\mathbf{r}) = \rho^\alpha(\mathbf{r}) - \rho^\beta(\mathbf{r})$ and the total electron density $\rho(\mathbf{r})$. Using the first choice, the total spin-polarized KS energy functional can be written (for an external magnetic field) as

$$E[\rho^\alpha, \rho^\beta] = T_s[\rho^\alpha, \rho^\beta] + V_{ne}[\rho^\alpha, \rho^\beta] + J[\rho^\alpha + \rho^\beta] + E_{xc}[\rho^\alpha, \rho^\beta], \qquad (3.14)$$

where

$$V_{ne}[\rho^\alpha, \rho^\beta] = \int d\mathbf{r}\Big[(v(\mathbf{r}) + \mu_B b(\mathbf{r}))\rho^\alpha(\mathbf{r}) + (v(\mathbf{r}) - \mu_B b(\mathbf{r}))\rho^\beta(\mathbf{r})\Big]. \qquad (3.15)$$

Above μ_B and $b(\mathbf{r})$ are the Bohr's magneton and the magnetic field in z-direction (simplification), respectively. The energy functional describing the Coulomb repulsion of electrons does not depend at all on the spin, and therefore the notation $J[\rho^\alpha + \rho^\beta]$ has been used.

Similarly as in the spin-independent case, the variational treatment of the Eq. (3.14) under charge and norm conservation constraints leads to the spin-dependent KS equations

$$\begin{aligned}
\Big[-\frac{1}{2}\nabla^2 + v^\alpha_{eff}(\mathbf{r})\Big]\phi_{i\alpha}(\mathbf{r}) &= \epsilon_{i\alpha}\phi_{i\alpha}(\mathbf{r}), \quad i = 1, 2, ..., N^\alpha \\
\Big[-\frac{1}{2}\nabla^2 + v^\beta_{eff}(\mathbf{r})\Big]\phi_{i\beta}(\mathbf{r}) &= \epsilon_{i\beta}\phi_{i\beta}(\mathbf{r}), \quad i = 1, 2, ..., N^\beta
\end{aligned} \qquad (3.16)$$

where the spin-dependent effective potentials are of the form

$$\begin{aligned}
v^\alpha_{eff}(\mathbf{r}) &= v(\mathbf{r}) + \mu_B b(\mathbf{r}) + \int \frac{\rho(\mathbf{r}')}{|\mathbf{r} - \mathbf{r}'|}d\mathbf{r}' + \frac{\delta E_{xc}[\rho^\alpha, \rho^\beta]}{\delta\rho^\alpha(\mathbf{r})} \\
v^\beta_{eff}(\mathbf{r}) &= v(\mathbf{r}) - \mu_B b(\mathbf{r}) + \int \frac{\rho(\mathbf{r}')}{|\mathbf{r} - \mathbf{r}'|}d\mathbf{r}' + \frac{\delta E_{xc}[\rho^\alpha, \rho^\beta]}{\delta\rho^\beta(\mathbf{r})}
\end{aligned} \qquad (3.17)$$

The electron numbers corresponding to the different spins

$$N^\alpha = \int d\mathbf{r}\rho^\alpha(\mathbf{r}), \quad N^\beta = \int d\mathbf{r}\rho^\beta(\mathbf{r}) \qquad (3.18)$$

have to be varied under constraint

$$N = N^\alpha + N^\beta \qquad (3.19)$$

in order to be able to determine the true total energy minimum of the system.

The spin-polarized KS method can describe many-electron system subjected to an external magnetic field. It is therefore possible to obtain information about the magnetic properties of the system such as e.g. the spin-susceptibility of electrons. Also the spin-orbit interaction and the other relativistic corrections can now be included into the theory. In addition, the description of systems without any external fields is also more accurate, because the exchange-correlation energy functional $E_{xc}[\rho^{\alpha}, \rho^{\beta}]$ has properties, which are missing in the spin-independent case. This is the situation especially for the open shell atoms, molecules and atomic clusters [30].

3.2 Local density approximation

It was shown in the previous section that using the KS method it is possible to calculate the exact $T_s[\rho]$. Nevertheless, in order to determine the exact KS equations it is necessary to know also the exact exchange-correlation functional $E_{xc}[\rho]$, which is the major challenge in the density functional theory. The magnitude of the exchange-correlation energy is relatively small with respect to the other terms in the energy functional (3.14). However, $E_{xc}[\rho]$ cannot be neglected since it has a crucial role in a reliable description of atomic clusters and molecules. It can e.g. affect the relative energy differences between various cluster isomers or molecular conformations.

First suggestion to the exchange-correlation problem was made by Kohn and Sham [8, 33], and it is called the local density approximation (LDA). Its spin-independent form is

$$E_{xc}^{LDA}[\rho] = \int \rho(\mathbf{r})\epsilon_{xc}(\rho)d\mathbf{r}, \tag{3.20}$$

where the function $\epsilon_{xc}(\rho)$ is the exchange-correlation energy of one electron in a homogeneous electron gas. In this equation it is assumed that the exchange-correlation energy of an inhomogeneous system can be obtained by using the results of the homogeneous electron gas for the infinitesimal parts of electron density. This treatment is not formally applicable for systems, where the electron density varies considerably (such as atoms and molecules), but in

practice it has been successfully used also for this kind of systems for many decades. Theoretical explanation for the success of LDA has been given in terms of so called exchange-correlation hole [7, 8, 30].

The exchange-correlation energy can be divided into two parts,

$$E_{xc}[\rho] = E_x[\rho] + E_c[\rho]. \tag{3.21}$$

The exchange energy $E_x[\rho]$ is in fact explicitly defined in the HF theory, and in the context of LDA it can be presented as

$$\begin{aligned} E_x[\rho] &= \int \rho(\mathbf{r})\epsilon_x(\rho)d\mathbf{r} \\ &= C_x \int [\rho(\mathbf{r})]^{4/3} d\mathbf{r}, \quad C_x = -\frac{3}{4}\left(\frac{3}{\pi}\right)^{1/3}, \end{aligned} \tag{3.22}$$

which was originally proposed by Dirac [49]. It is much harder to approximate the correlation energy $E_c[\rho]$ since the explicit form of this functional is not known.

The local density approximation can be straightforwardly expanded to a more accurate spin-dependent local spin density approximation (LSD). Also in this approximation, the exchange and correlation parts of the functional can be separated i.e.

$$E_{xc}[\rho^\alpha, \rho^\beta] = E_x[\rho^\alpha, \rho^\beta] + E_c[\rho^\alpha, \rho^\beta]. \tag{3.23}$$

By expanding Dirac's LDA exchange energy into the spin-polarized case [50], it is found that

$$E_x^{LSD}[\rho^\alpha, \rho^\beta] = 2^{1/3} C_x \int \left[(\rho^\alpha)^{4/3} + (\rho^\beta)^{4/3}\right] d\mathbf{r}. \tag{3.24}$$

Let us next define a spin-polarization parameter

$$\zeta = \frac{\rho^\alpha - \rho^\beta}{\rho^\alpha + \rho^\beta} = \frac{\rho^\alpha - \rho^\beta}{\rho}, \tag{3.25}$$

when consequently $\rho^\alpha = \frac{1}{2}(1+\zeta)\rho$ and $\rho^\beta = \frac{1}{2}(1-\zeta)\rho$. The LSD exchange energy is now

$$\begin{aligned} E_x^{LSD}[\rho^\alpha, \rho^\beta] &= \frac{1}{2} C_x \int \rho^{4/3} \left[(1+\zeta)^{4/3} + (1-\zeta)^{4/3}\right] d\mathbf{r} \\ &= \int \rho \epsilon_x(\rho, \zeta) d\mathbf{r}, \end{aligned} \tag{3.26}$$

where $\epsilon_x(\rho,\zeta)$ is the exchange energy per electron in a uniform electron gas with polarization ζ. It can be written as

$$\epsilon_x(\rho,\zeta) = \epsilon_x^0(\rho) + \left[\epsilon_x^1(\rho) - \epsilon_x^0(\rho)\right] f(\zeta). \tag{3.27}$$

The exchange energy per electron for the paramagnetic and ferromagnetic homogeneous electron density is

$$\epsilon_x^0(\rho) = \epsilon_x(\rho,0) = C_x\rho^{1/3}, \tag{3.28}$$
$$\epsilon_x^1(\rho) = \epsilon_x(\rho,1) = 2^{1/3}C_x\rho^{1/3}, \tag{3.29}$$

and the function, which describes the interval between these two cases, is

$$f(\zeta) = \frac{(1+\zeta)^{4/3} + (1-\zeta)^{4/3} - 2}{2(2^{1/3}-1)}. \tag{3.30}$$

On the contrary to the exchange energy, the correlation energy $E_c[\rho^\alpha,\rho^\beta]$ cannot be separated with respect to the spin-densities ρ^α and ρ^β since it contains both spin-dependent and spin-independent electron-electron interactions. Therefore, the presentation for the LSD correlation energy is

$$E_c^{LSD}[\rho^\alpha,\rho^\beta] = \int \rho\epsilon_c(\rho,\zeta)d\mathbf{r}, \tag{3.31}$$

where $\epsilon_c(\rho,\zeta)$ is the spin-dependent correlation energy per electron in a uniform electron gas. A discrete set of values has been calculated for $\epsilon_c(\rho,\zeta)$ by Ceperley and Alder [51] using the quantum Monte Carlo (QMC) method. Employing these numbers Vosko *et al.* [52] made a Padé approximative interpolation for $\epsilon_c(\rho,\zeta)$, which has been used very extensively in modern DFT studies.

Recently, many studies [53, 54, 55, 56] have been performed in order to improve LSD by introducing a further developed generalized gradient approximation (GGA), where the exchange-correlation energy functional is implicitly written as

$$E_{xc}^{GGA}[\rho^\alpha,\rho^\beta] = \int f(\rho^\alpha,\rho^\beta,\nabla\rho^\alpha,\nabla\rho^\beta)d\mathbf{r}. \tag{3.32}$$

The GGA methods take into account more rigorously the density variations of an inhomogeneous electron gas, and they consequently produce more accurate total and binding energies, as well as improved barriers to chemical reactions [57, 58]. Also the LSD lattice constants and bulk moduli of solids are improved [57]. Nevertheless, the ionization potentials and electron detachment energies are not necessarily better than in LSD [58].

3.3 Physical interpretation of the KS energy eigenvalues

In the Kohn-Sham method, the electron density is expressed in terms of auxiliary KS single-particle states in order to use the simple formalism of noninteracting case. Because of this purely artificial origin, KS states are not regarded as the real single-particle states of the system. However, in practice they are commonly treated and analyzed as real single-particle states since they show correct features. Similarly, the corresponding KS single-particle energy eigenvalues have been considered as auxiliary Lagrange multipliers without any physical meaning. It is shown in this chapter that there is indeed a well-defined physical relation concerning these energy eigenvalues called the Janak's theorem [24]. This theorem is based on a similar transition state approach of Slater [59].

The kinetic energy functional $T_s[\rho]$ in Eq. (3.5) is defined in such a manner that all the occupied KS states have a full occupation while the unoccupied states are completely empty. Let us next introduce a generalized kinetic energy

$$T_J[\rho] = \sum_{i=1} n_i \langle \psi_i | -\frac{1}{2}\nabla^2 | \psi_i \rangle, \tag{3.33}$$

where the occupation numbers n_i $(0 \leq n_i \leq 1)$ are varied in order to minimize the kinetic energy functional T_J. The corresponding electron density is now

$$\rho(\mathbf{r}) = \sum_{i=1} n_i |\psi_i(\mathbf{r})|^2, \tag{3.34}$$

where the electron spin is neglected at the moment. By replacing T_s with T_J in (3.6), the new (generalized) total-energy functional

$$E[\rho] = T_J[\rho] + V_{ne}[\rho] + J[\rho] + E_{xc}[\rho] \tag{3.35}$$

is achieved. One should note that the density ρ is given in terms of Eq. (3.34), and that the energy functional $E_{xc}[\rho]$ is modified due to the new definition of kinetic energy.

Let us now study the dependence of total energy on the occupation numbers by differentiating $E[\rho]$ with respect to n_i. After a few simple calculational

steps [24, 30] one obtains the result

$$\frac{\partial E}{\partial n_i} = \epsilon_i, \tag{3.36}$$

which is the important Janak's theorem. As it is clearly seen, this equation provides a meaning for the KS energy eigenvalues. It is important to emphasize here that the above result is derived for the KS method in general i.e. it does not depend on the explicit form of the exchange-correlation energy E_{xc}.

A direct consequence of the Janak's theorem (3.36) is that the ionization potential I and electron affinity A can be defined as integrals

$$-I = E_N - E_{N-1} = \int_0^1 \epsilon_{HOMO}(n)dn, \tag{3.37}$$

$$-A = E_{N+1} - E_N = \int_0^1 \epsilon_{LUMO}(n)dn, \tag{3.38}$$

where the KS energy eigenvalues ϵ_{HOMO} and ϵ_{LUMO} corresponding to the highest occupied (HOMO) and lowest unoccupied (LUMO) KS state are now determined also for the noninteger occupations. Alternatively, one can also use numerically approximative formulas

$$-I = E_N - E_{N-1} \approx \epsilon_{HOMO}(1/2), \tag{3.39}$$

$$-A = E_{N+1} - E_N \approx \epsilon_{LUMO}(1/2), \tag{3.40}$$

which of course are not physically realistic. The other way to express these equations in a physically more reasonable form is

$$-I = E_N - E_{N-1} = \epsilon_{HOMO}(1) - C, \tag{3.41}$$

$$-A = E_{N+1} - E_N = \epsilon_{LUMO}(0) + D, \tag{3.42}$$

where the positive constants C and D have to be determined separately for each specific system. One should note that without these additional constants equations (3.41) and (3.42) are just the Koopmans' theorem for Hartree-Fock single-particle energy eigenvalues.

A more illustrative way to build a connection between the ionization potential and the KS energy eigenvalue of the HOMO state is to follow the work of Tozer and Handy [60]. According to them, the ionization potential can be written as a generalized Koopmans' theorem (GKT)

$$-I_{GKT}(N) = \epsilon_{HOMO}(N) - v_{xc}^{\infty}(N), \tag{3.43}$$

where $v_{xc}^{\infty}(N)$ is the asymptotic limit of the exchange-correlation potential of an N-electron system. It is evident, that $v_{xc}^{\infty}(N)$ is the undetermined energy shift C in Eq. (3.41). Perdew *et al.* [61] have shown that for a real energy functional, where the electron number increases through integers, $v_{xc}^{\infty}(N)$ should be zero. In practice, the used density functionals are however continuous, which leads to a nonzero energy shift $v_{xc}^{\infty}(N)$ [57, 62].

3.4 BO-LSD-MD method

The method used throughout this thesis is the Born-Oppenheimer local-spin-density molecular dynamics (BO-LSD-MD) method created by Barnett and Landman, and fully documented in Ref. [13]. In the BO-LSD-MD method, the ions move on the Born-Oppenheimer potential energy surface where the description of the electronic structure is based on LSD, in conjunction with separable nonlocal norm-conserving pseudopotentials [37], and a plane wave basis set. Evaluations of the various terms in the Hamiltonian, and the operations on the KS wave functions, are performed using a dual-space formalism, where the calculations are carried out using both real and reciprocal spaces. This method was developed for the investigations of finite aggregates causing it to differ remarkably from the other BO dynamical simulation methods. Especially, the method does not employ a supershell replication procedure (i.e. periodic boundary conditions), and therefore there are no repeated images of the system. This allows one to study effectively charged systems and systems possessing large multipole moments. Furthermore, the ground state electronic energy and forces on the ions are calculated for each nuclear configuration during a dynamical simulation. This allows a relatively large time step, $\tau \approx 1 - 10$ fs, for the integration of ionic equations of motion, the limiting time scale arising from the real ion dynamics and from the performance of the MD integration algorithm.

According to the BO approximation, the total energy of a system consisting of ions and valence electrons can be presented as

$$E_{total}(\{\mathbf{R}_A\}, \{\dot{\mathbf{R}}_A\}) = \sum_A \frac{1}{2} M_A |\dot{\mathbf{R}}_A|^2 + \sum_{B>A} \frac{Z_A Z_B}{R_{AB}} + E_{elec}(\{\mathbf{R}_A\}), \quad (3.44)$$

where $\mathbf{R}_A$, M_A and Z_A are the position, mass and charge of the Ath ion,

respectively, and $E_{elec}(\{\mathbf{R}_A\})$ is the total energy of valence electrons determined for a specific ionic configuration $\{\mathbf{R}_A\}$. The first two terms in Eq. (3.44) represent the ionic kinetic energy and the coulombic interaction energy between ions, respectively.

As pointed out in Chap. 2, the main problem in Eq. (3.44) is to calculate the electronic ground state energy $E_{elec}(\{\mathbf{R}_A\})$, which in this method is computed via KS method and LSD parametrization for the exchange-correlation part of the electron-electron interaction energy. The corresponding ground state energy is now given by the formula

$$E_{elec}[\rho^\alpha, \rho^\beta] = T_s[\rho^\alpha, \rho^\beta] + V_{ne}[\rho^\alpha, \rho^\beta] + V_{ee}[\rho^\alpha, \rho^\beta], \tag{3.45}$$

where T_s is the kinetic energy of electrons, V_{ne} is the electron-ion interaction energy, with the interaction potential between valence electrons and ions described by pseudopotentials, and V_{ee} is the electron-electron interaction energy. The evaluation of these three terms is discussed below.

As previously discussed in the context of KS method, the kinetic energy T_s is written as

$$T_s = \sum_{i,\sigma} n_{i\sigma} \langle \psi_{i\sigma} | T | \psi_{i\sigma} \rangle, \tag{3.46}$$

where σ is the spin index. The kinetic energy operator $T = -\frac{1}{2}\nabla^2$ is diagonal in momentum space. Therefore, also the kinetic energy is computed in momentum space. The occupation numbers $n_{i\sigma}$ are usually integers 0 or 1, but if the HOMO-LUMO gap is very small, it may be necessary to use fractional occupation numbers in order to achieve self-consistency. For this kind of situations a Fermi function with $k_B T = 0.0005$ a.u. is used.

The electron-ion interaction is described using separable nonlocal norm-conserving pseudopotentials [37] as

$$V_{ne} = \sum_{i,\sigma} n_{i\sigma} \sum_A \langle \psi_{i\sigma} | V_A | \psi_{i\sigma} \rangle. \tag{3.47}$$

In real space the pseudopotentials can be separated into local and nonlocal parts

$$V_A(\mathbf{R}_A; \mathbf{r}, \mathbf{r}') = V_A^{lc}(|\mathbf{r} - \mathbf{R}_A|)\delta(\mathbf{r} - \mathbf{r}') + V_A^{nlc}(\mathbf{r} - \mathbf{R}_A, \mathbf{r}' - \mathbf{R}_A). \tag{3.48}$$

The nonlocal term is obtained from a semiclassical pseudopotential via Kleinman-Bylander prescription [63]

$$V_A^{nlc}(\mathbf{r},\mathbf{r}') = \sum_{l,m} F_l^A K_{lm}^A(\mathbf{r}) K_{lm}^A(\mathbf{r}'), \tag{3.49}$$

where the ion is at the origin, and

$$K_{lm}^A(\mathbf{r}) = \Delta V_l^A(r) R_l^A(r) Y_{lm}(\hat{r}), \tag{3.50}$$

$$F_l^A = \left(\int_0^\infty dr \left[r R_l^A(r) \right]^2 \Delta V_l^A(r) \right)^{-1}. \tag{3.51}$$

Here $\Delta V_l^A(r)$ is the semilocal pseudopotential and $R_l^A(r)$ is the radial pseudowave function.

In order to evaluate the effective KS single-particle potential

$$v_\sigma = \frac{\delta E_{elec}}{\delta \rho_\sigma} - \frac{\delta T_s}{\delta \rho_\sigma} \tag{3.52}$$

conveniently, it is necessary to divide the energy functional V_{ne} into local and nonlocal parts

$$V_{ne}^{lc} = \int d\mathbf{r} [\rho^\alpha + \rho^\beta] \sum_A V_A^{lc}(|\mathbf{r} - \mathbf{R}_A|) \tag{3.53}$$

and

$$V_{ne}^{nlc} = \sum_{i,\sigma} n_{i\sigma} \sum_{A,l,m} F_l^A \left| \int d\mathbf{r} K_{lm}^A(\mathbf{r} - \mathbf{R}_A) \psi_{i\sigma}(\mathbf{r}) \right|^2. \tag{3.54}$$

The contribution of the local term is now

$$v_{ne}^{lc}(\mathbf{r}) = \frac{\delta V_{ne}^{lc}}{\delta \rho_\sigma(\mathbf{r})} = \sum_A V_A^{lc}(|\mathbf{r} - \mathbf{R}_A|), \tag{3.55}$$

and it can be combined with the LSD potential considered below. The nonlocal KS potential is

$$v_{ne}^{nlc}(\mathbf{r},\mathbf{r}') = \sum_A V_A^{nlc}(\mathbf{r} - \mathbf{R}_A, \mathbf{r}' - \mathbf{R}_A), \tag{3.56}$$

where V_A^{nlc} is evaluated above (equations (3.49)-(3.51)).

The electron-electron interaction functional is given by

$$\begin{aligned} V_{ee}[\rho^\alpha, \rho^\beta] &= J[\rho^\alpha, \rho^\beta] + E_{xc}[\rho^\alpha, \rho^\beta] \\ &= \int d\mathbf{r} [\rho^\alpha(\mathbf{r}) + \rho^\beta(\mathbf{r})][\epsilon_H(\mathbf{r}) + \epsilon_{xc}(\mathbf{r})], \end{aligned} \tag{3.57}$$

where

$$\epsilon_H(\mathbf{r}) = \frac{1}{2}\int d\mathbf{r}' \frac{\rho^\alpha(\mathbf{r}') + \rho^\beta(\mathbf{r}')}{|\mathbf{r} - \mathbf{r}'|} \tag{3.58}$$

is the Hartree component of energy density, which describes the coulomb interaction between electrons, and

$$\epsilon_{xc}(\mathbf{r}) = e_{xc}[\rho^\alpha(\mathbf{r}), \rho^\beta(\mathbf{r}); \nabla\rho^\alpha(\mathbf{r}), \nabla\rho^\beta(\mathbf{r})] \tag{3.59}$$

is the exchange-correlation energy per electron. As discussed previously, in LSD approximation ϵ_{xc} depends solely on the electron density and is simply the exchange-correlation energy per electron of a uniform electron gas with densities ρ^α and ρ^β. The LSD parametrization for the exchange part is presented in Eq. (3.27), and the LSD correlation part is the aforementioned (see Sec. 3.2) parametrization by Vosko et al. [52]. It is also possible to include the gradient corrections into the exchange-correlation energy (3.59) although they have a very minor role in this thesis. The method uses the exchange-gradient correction of Becke [55] and the correlation-gradient correction of Perdew [53]. These corrections are added in a post-LSD fashion i.e. the gradient correction to the energy is calculated non-self-consistently for a LSD-generated density. Although this approach has been successful in practice, one has to remember that the post-LSD gradient corrections are not determined at the true GGA ground state[1].

The electron-electron part of the effective KS single-particle potential at LSD level is now

$$v_\sigma^{LSD}(\mathbf{r}) = \frac{\delta V_{ee}}{\delta\rho_\sigma(\mathbf{r})} = 2\epsilon_H(\mathbf{r}) + \left[1 + \rho_\sigma(\mathbf{r})\frac{\partial}{\partial\rho_\sigma(\mathbf{r})}\right] e_{xc}[\rho^\alpha(\mathbf{r}), \rho^\beta(\mathbf{r})], \tag{3.60}$$

where ϵ_H is presented above, and the derivatives of ϵ_{xc} have been published in Ref. [52].

Finally, the calculations involving classical dynamics of ions on the BO potential energy surface require evaluation of force on each ion. The electronic force obtained using the Hellmann-Feynman theorem (see Sec. 2.1), together with the coulombic repulsion of ions, governs now the dynamical evolution of ions generated via integration of the Newtonian equations of motion

$$M_A\ddot{\mathbf{R}}_A = -\nabla_{\mathbf{R}_A} V_{ne}(\{\mathbf{R}_A\}) - \nabla_{\mathbf{R}_A}\left[\sum_{B>A} \frac{Z_A Z_B}{|\mathbf{R}_A - \mathbf{R}_B|}\right] \tag{3.61}$$

[1] The most recent implementation of the method uses the PBE parametrization [56] for the gradient-corrected exchange-correlation energy at the true GGA ground state.

It is necessary to note here that the electronic contribution in Eq. (3.61) differs from the original Hellmann-Feynman theorem in the sense that it is divided into two parts, local and nonlocal, due to the separability of pseudopotentials.

Chapter 4

Main results

4.1 Small aluminum clusters

The number of local potential energy minima on a potential energy surface of ions grows rapidly (~exponentially [64]), when the number of constituent ions increases. The search for the global energy minimum (ground state) among these different ionic configurations (isomers) is one of the most challenging and fascinating tasks in the modern cluster research since the detailed description of clusters is strongly related to the properties of the corresponding ground state. Furthermore, theoretical investigations are in a crucial role in this field, because it is still not possible to determine directly the ground state geometries of small clusters in experiments.

In this section, the results for the small aluminum clusters are presented. The structures were obtained for Al_2 to Al_7 by a conjugate-gradient search among a number of plausible candidates. For the size-range Al_{12}–Al_{23} a classical molecular dynamics program was used in conjunction with a potential derived from the effective medium theory (EMT) [65, 66] to produce a number of low-energy isomers, the best ones of which were selected as starting geometries for the BO-LSD-MD calculations. The structures were obtained by cooling from hot liquid clusters. The vast number of the lowest energy structures produced by EMT potential were icosahedral-based structures. As it is well

Table 4.1: Symmetry, cohesive energy per atom (in eV), average bond length (in Å), experimental [15] and calculated vertical (vIP) and adiabatic (aIP) ionization potential (in eV) for ground states of Al–Al_7.

N	Symm	$E_C(LSD)$	⟨d⟩	IP(exp)	vIP(LSD)	aIP(LSD)
1				5.99	6.12	
2	D_∞	0.96	2.46	6.20	6.83	6.25
3	C_{3v}	1.60	2.48	6.45	6.91	6.79
4	D_{2h}	1.84	2.58	6.55	6.80	6.69
5	C_{2v}	2.11	2.58	6.45	6.77	6.68
6	O	2.33	2.73	6.45	7.03	6.93
7	O	2.56	2.69	6.20	6.38	5.90

known, certain sizes (13,19,23) are particularly interesting since they match filled atomic-shell structures of either icosahedral, decahedral or FCC-based ((cub)octahedral) symmetry (see Fig. 4.1). For these sizes optimization was started directly from these symmetries. All the structure optimizations were done without any constraints to the symmetry.

The ground state structures, binding energies, average bond lengths and ionization potentials[1] for Al–Al_7 are given in Table 4.1. The experimental ionization potentials are from the paper of Schriver *et. al.* [15]. The total spins of these clusters (both neutral and ionic) were found to be minimal i.e. $S = 0$ or $S = \frac{1}{2}$ for a cluster with even and odd number of electrons, respectively. The only exceptions are the dimer and, in a larger size range, the Al_{13} ion (icosahedron) with $S = 1$. In fact, the nonparamagnetic nature of Al dimer has been observed also experimentally [16], and it has been suggested previously also by other theoretical studies [20, 21]. Furthermore, the obtained bond length for the dimer is the same (within 0.01 Å) as the experimental one [67]. This gives an indication that the used aluminum pseudopotential [37] in combination with LSD works well.

In Figure 4.1, closed atomic shell structures for 13, 19 and 23 atoms are displayed. Several previous calculations [11, 12, 23] have addressed the question

[1]The ionization potentials are calculated as total energy differences between the cluster and the corresponding unrelaxed/relaxed ion.

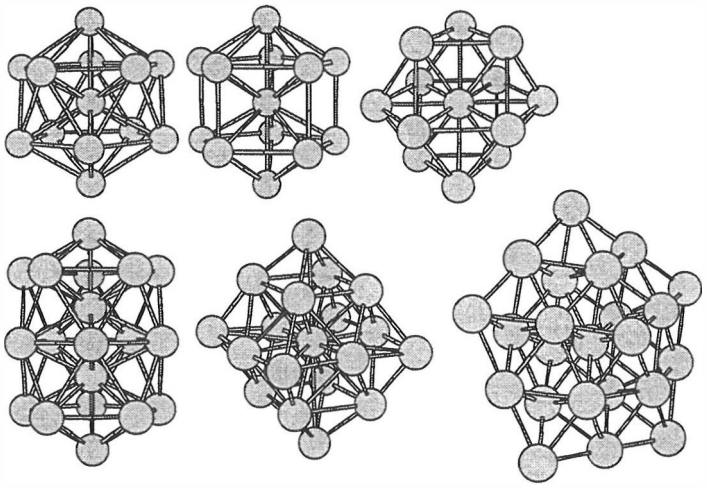

Figure 4.1: Closed atomic shell structures. Top from left: 13-atom icosahedron, truncated decahedron, and cubo-octahedron. Bottom: 19-atom double icosahedron, octahedron, and 23-atom decahedron.

in what size region FCC-based structures become energetically competitive with icosahedral structures. In agreement with these previous calculations, it is found that Al_{13} clearly prefers icosahedron (ICS) over cubo-octahedron (COS). In fact, 13-atom COS transforms to ICS in molecular dynamics runs at low temperature (< 100 K). In the size range of $14 \leq N \leq 23$ there are certain sizes (17,19,21) where icosahedral stacking slightly wins FCC-based structures in energy, whence for Al_{18} FCC-isomer is notably energetically favourable. Especially interesting is the case of Al_{19}, where both double icosahedron and octahedron are closed atomic shell structures (Fig. 4.1). The total energy difference for these structures is only 60 K[2]. The decahedral isomers are surprisingly close to the icosahedral ones for $N = 13 - 15$, and are *the best* structures for $N = 22, 23$.

The adiabatic ionization potential (aIP) of small aluminum clusters is displayed in Figure 4.2 together with the experimental results [15]. Having in mind that in the experiment (i) IP is determined from the threshold energy and (ii) the temperature of clusters is fairly low, the following criterion is used: For a comparison with the experiment, the *lower* calculated aIP of the

[2]Here the total energy difference is converted to vibrational motion of ions via classical equipartition theorem and taking into account the $3N - 6$ degrees of freedom.

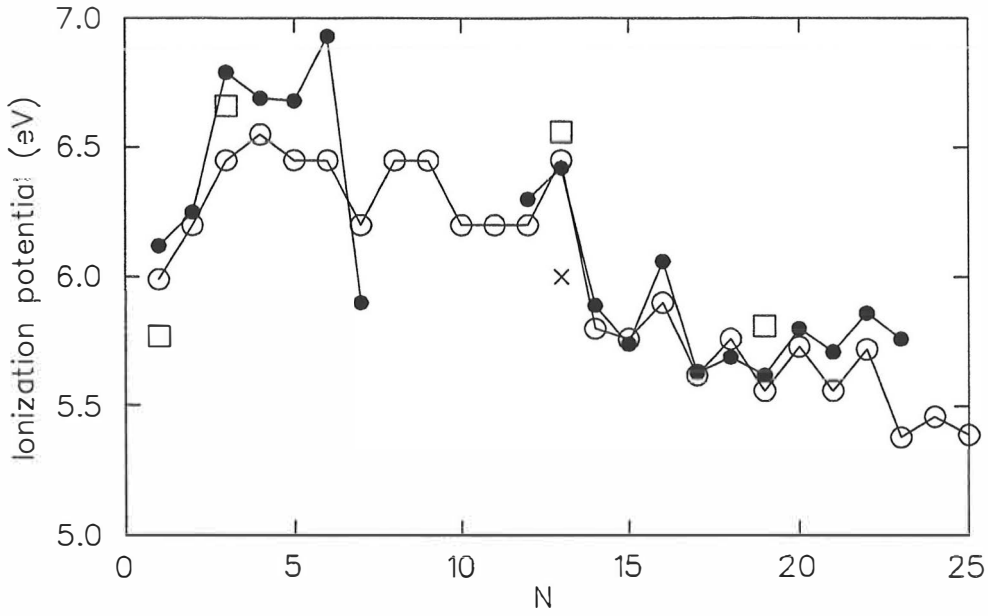

Figure 4.2: Ionization potential of aluminum clusters (in eV). Open circles: threshold photoionization experiment [15], solid dots: BO-LSD-MD results, open squares: Car-Parrinello calculations [11], and crosses: DVM $X\alpha$ results [12].

co-existing structures within 150 K in energy should determine the threshold energy. Otherwise, the aIP of the ground state (as in the cases Al–Al_7) is plotted in Fig. 4.2. This simple criterion produces a surprisingly good agreement with the measurement in the size-range ($12 \leq N \leq 23$), and it can be interpreted as an indirect evidence that for this size region the competition between different structures becomes important. For the smaller clusters the comparison is not as successful. This might be due to less accurately determined experimental values (so called bracketing method), and also, on the theoretical side, the applicability of aIP in the smaller size range, where the electronical relaxation due to the ionization can cause drastic effects, is questionable. It should be emphasized here that no attempts have been made yet to estimate the effect of temperature on the IP (see Sec. 4.2).

It has been observed both experimentally and theoretically [18, 48, 68, 69, 70] that the IP of alkali clusters behaves quite consistently according to the formula

$$I = W + \alpha \frac{e^2}{R}, \tag{4.1}$$

where W is the bulk work function and R is the radius of the (spherical) cluster. This equation is a result for a finite classical metal sphere, where $\alpha = \frac{1}{2}$. The same equation applies also in the jellium model, but the value of coefficient α is different. From Fig. 4.2 it is seen that small aluminum clusters do not behave consistently with the above model. Especially remarkable is that there is an initial rise of IP starting from Al atom, which is in total contradiction with Eq. (4.1). Furthermore, strong deviations from the $\propto \frac{e^2}{R}$ behaviour are seen up to $N \approx 20$, and even beyond. The probable explanation for the behaviour of IP for small N is an incomplete $s-p$ hybridization.

In order to analyze the hybridization effects for the smallest clusters, each occupied KS state, ψ_i^{KS}, was projected onto spherical harmonic components according to

$$\psi_i^{KS}(\mathbf{r}) = \sum_{\ell,m} \phi_{\ell,m}^i(r) Y_{\ell,m}(\Omega)\,, \tag{4.2}$$

with ℓ up to 3 (atomic f-state), from which a weight w_ℓ^i of a given angular momentum component in the charge density is

$$w_\ell^i = \sum_{m=-\ell}^{\ell} \int [\phi_{\ell,m}^i(r)]^2 r^2 dr. \tag{4.3}$$

This analysis was performed from dimer to tetramer the origin for the expansion (4.2) set at the atoms. It is important to mention here that the plane wave basis set prevents in this context a full Mulliken analysis common in traditional quantum chemistry. However, it is seen here that the average weight $\bar{w}_l$ (over all atoms in the cluster) provides useful information on the degree of hybridization of a given KS state, which qualitatively agrees with earlier quantum-chemical results [21]. According to the molecular orbital theory, four lowest and two highest states (including spin) of the dimer should derive from atomic $3s$ and $3p$ states, respectively. Indeed, it was found that for the four lowest states $\bar{w}_s = 0.85 - 0.87$ and $\bar{w}_p = 0.11 - 0.14$, whence the two highest states are clearly p-dominated with $\bar{w}_p = 0.95$. For the trimer, the primary components are $\bar{w}_s = 0.61 - 0.83$ for the six lowest states and $\bar{w}_p = 0.93 - 0.97$ for the remaining three states. Most of the states for the tetramer are already heavily $s-p$ mixed. As seen from Table 4.1, the calculated IP initially rises up to Al_3, leveling off after that, exhibiting a strong drop from Al_6 to Al_7. The leveling off happens around the size where $s-p$ hybridization starts according to the above analysis.

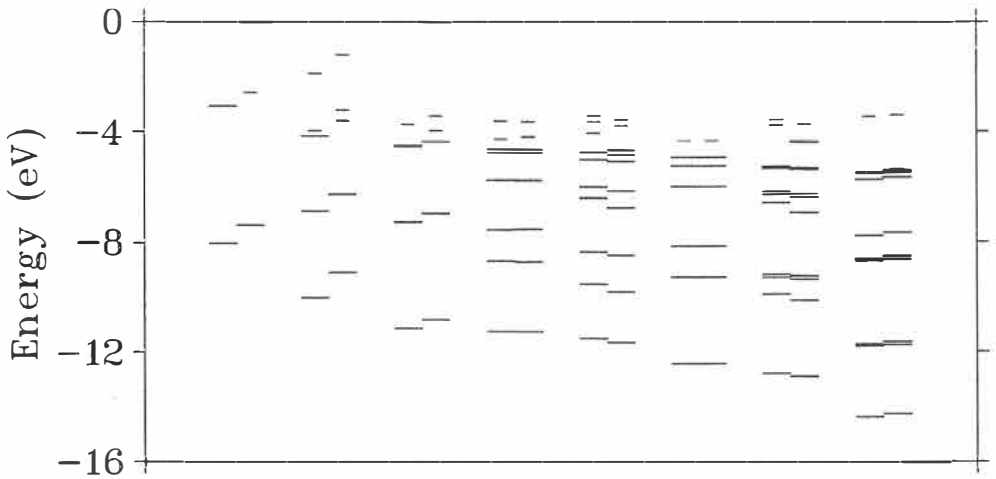

Figure 4.3: Kohn-Sham one-electron eigenvalues (in eV) for selected ground-state Al_N clusters. From left: Al atom, Al_2–Al_7, and icosahedral Al_{13}. The longer and shorter lines correspond to occupied and unoccupied levels, respectively. Also the spin splitting is shown.

The high IP's for Al_6 and Al_{13} can be associated to jellium-type shell effects. As seen from Figure 4.3, Al_6 and Al_{13} show a fairly nicely grouped level structure, and having 18 and 39 electrons, respectively, are close to magic numbers of spherical jellium. The angular momentum analysis has been performed also for these clusters, but now the origin for the expansion (4.2) was set to the center of electronic charge density of the cluster. The analysis results in the sequence $1s^2 1p^6 1d^4 (2s1d)^2 1d^4$ for the occupied states of Al_6. Each angular momentum component has a weight of at least 0.94, except the mixed (2s1d) state where the primary weights are $w_s = 0.80$ and $w_d = 0.12$. Al_{13} has a clear jellium-type sequence $1s^2 1p^6 1d^{10} 2s^2$ for the 20 lowest states. The highest occupied shell has a strong $p-f$ mixing which is understandable since the five-fold symmetry of icosahedron is known to split $\ell = 3$ orbitals. Al_6 and Al_{13} thus appear to exhibit surprisingly well-defined jellium-type shell structure. The strong drops in IP from Al_6 to Al_7 and from Al_{13} to Al_{14} thus reflect HOMO states of Al_7 (seen in Fig. 4.3) and Al_{14} that are above the jellium gaps at 20 and 40 electrons, respectively.

The calculated cohesive energies $E_c(N) = -(E(\mathrm{Al}_N) - NE(\mathrm{Al}))/N$ updated with the most recent calculations for Al_{36}–Al_{102} were already shown in Figure 1.1 together with some other DFT calculations[11, 12] and data from photodissociation experiments by Ray *et. al.* [10]. The BO-LSD-MD results are generally consistent with other DFT studies being 0.2–0.5 eV higher than

experimental values, a behaviour typical to DFT with local density approximation. The post-LSD gradient correction (Sec. 3.4) has been calculated for some of the clusters, and its effect is to lower the LSD cohesive energy. For instance, in the size range Al_{20}–Al_{23}, this effect is averagely 0.50 eV giving E_C values in a good agreement with the experiments. The important feature portrayed by Figure 1.1 is the fact that the experimentally determined cohesive energies even from Al_7 seem to linearly extrapolate quite reasonably to the known bulk cohesive energy, and a similar trend is seen in the calculated values from Al_{12} on, though the prediction for the bulk cohesive energy is now overestimated due to LSD.

4.2 Temperature effects on ionization potential of clusters

Although the definition of ionization potential is a simple one, the determination of clusters' IP values from the experimental photoionization efficiency (PIE) curve has been difficult due to the thermal and quantum mechanical effects. These effects are related to the experimental conditions, where there is always a finite temperature, and to the ionization process itself, which involves an incoming photon and an outgoing photoelectron. Consequently, thermal tails and local maxima are observed in the PIE curve. In this section these effects are discussed. It is important to emphasize that the following treatment does not include any plasmon effects (i.e. a single-particle picture is used for electrons) and photoinduced fragmentation of clusters. In addition, the ionization process is considered here as a vertical process for two reasons. Firstly, from a simple classical point of view, the ionization process is too fast to include ionic relaxation, and secondly, the concept adiabatic IP loses its meaning at a finite temperature.

In order to study the temperature-dependent ionization potential of clusters and molecules, one has to perform molecular dynamics and calculate the ionization potentials for the whole set of recorded ionic configurations. Within the BO-LSD-MD method, which is especially designed for finite systems, this can be done by calculating the total energy differences $I = E_{N-1} - E_N$ for each configuration and corresponding converged electron densities. However, in practice this is a very elaborate process and other alternatives have to be

considered. In this thesis a major emphasis is put on the Janak's theorem (Sec. 3.3) and the consequent GKT formula (3.43), which introduces a connection between the IP and the highest occupied KS state. In principle, this does not alleviate the IP problem, since one has to still calculate the asymptotic exchange-correlation potential $v_{xc}^{\infty}(N) = E(N-1) - E(N) + \epsilon_{HOMO}(N)$ for each time step, separately. However, during the studies of this thesis it became evident that at least for aluminum and sodium $v_{xc}^{\infty}(N)$ does not depend on the geometry of a particular cluster. For instance, for different Al_6 and Al_7 isomers these values where within 0.1 eV while the deviation of IP values was about 0.6-0.8 eV. Thus, it should be clear that the temperature-dependent IP problem becomes much easier, if one uses in Eq. (3.43) the mean value of $v_{xc}^{\infty}(N)$, which has been calculated for a certain set of different isomers. Consequently, it is now possible to simulate the IP distributions of clusters at various temperatures with a relatively little effort.

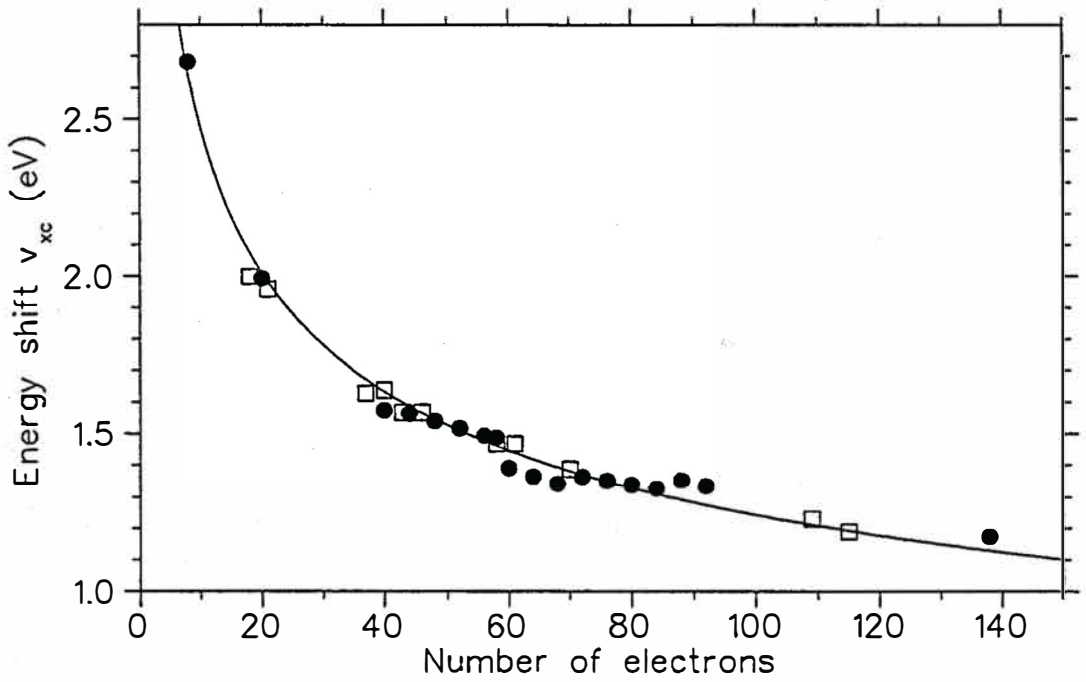

Figure 4.4: The calculated energy shift v_{xc}^{∞} of aluminum clusters as a function of valence electron number. The open squares correspond to the BO-LSD-MD results calculated using LSD approximation for $N_e < 50$ and LDA approximation for the larger electron numbers. The filled spheres correspond to the spherical jellium results calculated using LDA approximation. The curve is fitted to the jellium results.

The calculated LDA/LSD mean values of v_{xc}^{∞} for Al clusters are presented in Figure 4.4. Also the values obtained using the spherically constrained jellium model and LDA approximation are presented. A curve $v_{xc}^{\infty} = cN^{\alpha}$ is fitted to

the jellium results, resulting $\alpha = -0.299$ for aluminum ($r_s = 2.07$). As one can see, the BO-LSD-MD and jellium results are very similar, although the values of ionization potential are known to differ considerably between these two models. Also the asymptotically decreasing trend of v_{xc}^{∞} as a function of electron number is very clear. Indeed, the exponent of the fitting curve is very close to the value $-\frac{1}{3}$, which means that v_{xc}^{∞} is inversely proportional to the mean radius R of the cluster. This is also the classical behaviour for the ionization potential of metal clusters. However, one must remember that IP approaches the bulk work function when N increases, whereas v_{xc}^{∞} approaches zero. In addition, it should be stressed that the magnitude of energy shift v_{xc}^{∞} for a given cluster size depends crucially on the used exchange-correlation energy functional.

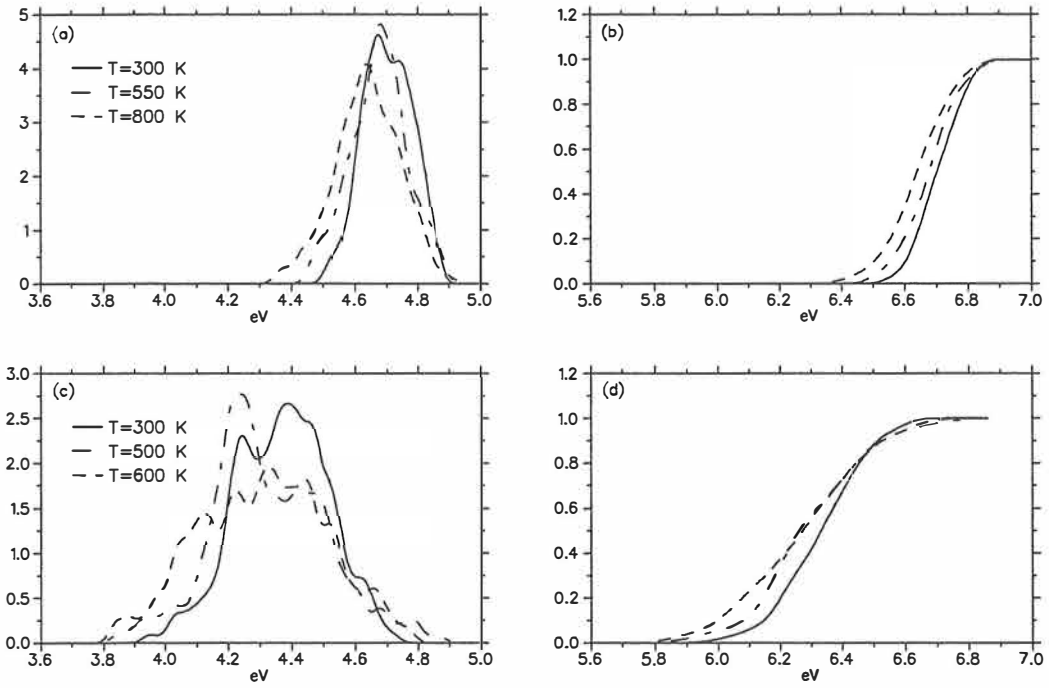

Figure 4.5: Distributions of the HOMO level (absolute value) and corresponding PIE curves at different temperatures. (a) HOMO level distribution and (b) PIE curve of Al_6; (c) HOMO level distribution and (d) PIE curve of Al_7.

In practice, when the energy shift v_{xc}^{∞} is known, it is possible to obtain the IP distribution. Furthermore, by integrating this distribution one obtains the threshold of the theoretical PIE curve, where only the HOMO state is considered at the moment. In Figure 4.5 this is demonstrated by plotting the HOMO level (absolute value) distributions and the corresponding PIE

curves for Al_6 and Al_7 at different temperatures. The differences between these two clusters are obvious: the distributions of Al_7 are remarkably wider and the mean values of the distributions differ more than 0.2 eV. Another difference is that the upper boundary of the distribution of Al_7 moves to a higher energy when the temperature is increased, while the distribution of Al_6 seems to have a fixed upper boundary, which corresponds to the KS energy of the ground state. One should note that the oscillations of the distributions have a purely statistical origin due to the shortness of MD runs (4-5 ps). The width of the distribution for both clusters is proportional to $T^{1/2}$ as expected from the nearly harmonic motion of the ions.

The different behaviour of PIE curves of Al_6 and Al_7 is understandable in terms of the jellium model, where 20 valence electrons correspond to a full electron shell. For Al_7 there is only one electron in the uppermost shell. This less bound electron is more sensitive to the geometry changes causing a notable thermal tail in the threshold of the PIE curve. This is fully consistent with the experimental PIE curves of small alkali metal clusters at a finite temperature [68, 70].

There are several ways to extract the ionization potential from the PIE curve [68, 70, 71]. Usually, the IP value is determined from the threshold using so called baseline intercept method [68]. Fig. 4.5 illustrates that the value obtained from the threshold does not correspond to the calculated vIP value of the ground state (see Table 4.1), which it underestimates. Actually, a good correspondence between the aIP and the experimental threshold IP has been observed in many cases. However, these two are not directly related to each other, and in some cases this connection breaks down. For Al_7 this is seen in Fig. 4.2, where the obtained aIP is well below the experimental value because of the strong relaxation of Al_7^+ ion. Furthermore, the discrepancy between the theoretical and experimental IP values for Al_6 and Al_7 in Fig. 4.5 can now be solved by taking into account the experimental temperature (room temperature) and the method used to extract the ionization potential (bracketing). The theoretical IP thresholds of these two clusters now coincide with the experimental values.

The method presented so far has one limitation. It presumes that the cross section of the HOMO state is a constant regardless of the energy and symmetry of the single-particle state. In practice [47, 68, 70], it has been however noticed that the PIE curves often decay exponentially after they have reached

a local maximum. In order to take this effect into account, a semiempirical modification is introduced, where during the integration of IP distribution, the HOMO level energies are weighted by an exponential step function

$$w_i(E) = e^{-\alpha(E-E_i)}\theta(E - E_i), \tag{4.4}$$

where $\theta(E-E_i)$ is the Heaviside's step function. The value of α is determined from the experimental PIE curve.

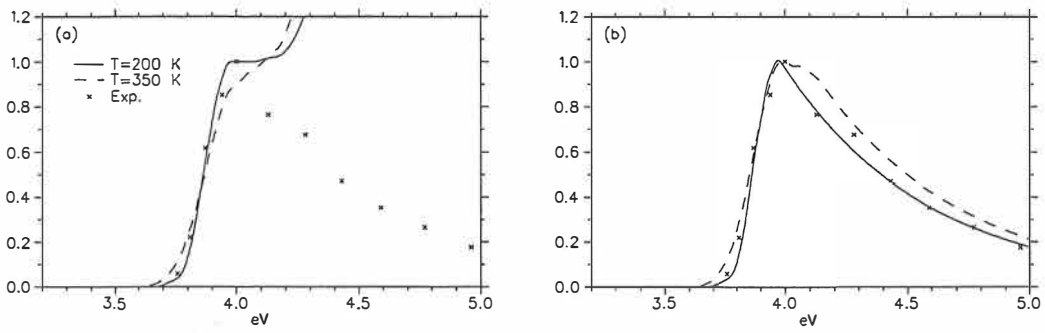

Figure 4.6: Theoretically determined PIE curves for Na_{10} at different temperatures compared to the experiments (crosses) [70]. (a) Heaviside's step function and (b) exponentially decaying step function are used in integration. The real theoretical curves are shifted by 0.23 eV in order to make the comparison to the experiments easier.

The integrated IP distributions of Na_{10} are presented in Figure 4.6. For comparison, these distributions are shifted with respect to the experiments[3]. The experimental points represent mean values of the fluctuating signal, which are small close to the threshold and increase with increasing energy. Two different weights are used in integration: (a) a normal step function and (b) an exponentially decaying step function. One should note that also the inner single-particle states are taken into account in (a). The exponent parameter α in Eq. (4.4) is obtained from the experimental PIE values [70] presented in Figure 4.6. By comparing Figures 4.6(a) and 4.6(b), one can see that the rising part of the PIE curve (where the experiment is more accurate) does not depend on the weighting procedure, which makes our exponential step function method compatible with the unweighted procedure. Furthermore, the HOMO state of Na_{10} is well separated from the underlying states, which is consistent with the spherical jellium model. This confirms that for Na_{10} it is reasonable to determine the PIE curve using the HOMO state alone.

[3]Within the BO-LSD-MD method the IP values of Na clusters are systematically too large because of the used pseudopotential and LDA.

A considerable consistence with the experiments [70] at 200 K is seen from both of the Figures 4.6(a) and 4.6(b). It should also be noted that the experimental point around 4.2 eV, which does not fit into the theoretical curve, corresponds actually to the energy where the next underlying state starts to contribute, if it is assumed that the separation between the two highest KS states is the same as for the real single-particle states. Also in Fig. 4.6(b) the thermal broadening of the PIE curve is clearly seen. At 350 K the theoretical curve is definitely too wide and the slope of the rising part is too small. It is easy to conclude that a very good fit to the experiments (cluster temperature unknown) is obtained at 200 K.

Usually, it is necessary to consider also the innercore ionization in order to calculate the post-threshold regions of the PIE curve. In the model described above, this can be done using the same energy shift v_{xc}^{∞}, which was calculated for the HOMO state, also for the inner KS states, and integrating over these energies using the semiempirical weighting of Eq. (4.4). The theoretical justification for the innercore v_{xc}^{∞} shift exists, and it is presented in the next section. On the contrary, the weighting procedure does not stand on a solid theoretical ground, since in this context it is assumed that the electric dipole (E1) transition matrix elements are the same for all the considered states. Therefore, within this frame of reference, one can only study the applicability of this method in comparison with the experiments. In practice, this treatment appeared to be applicable for other small sodium clusters ($N = 8, 14, 20$), where also the underlying states had to be considered.

4.3 Photoelectron spectroscopy of aluminum cluster anions

Photoelectron spectroscopy is a rich source of information pertaining to the electronic structure and excitation spectra of atoms, molecules, and condensed phases. Atomic clusters exhibit a high sensitivity of the electronic spectrum to the geometrical structure, which often differs that from the bulk. Consequently, high-resolution photoelectron spectroscopy emerges as an important tool in cluster science, particularly in the face of several difficulties in applying common direct structure determination techniques to such systems.

In this section the emphasis of the discussion is on the theoretical simulation of the photoelectron spectrum (PES) via density functional theory and BO-LSD-MD method. Similar investigations have been pursued previously using both quantum-chemical [72, 73] and DFT methods [74, 75]. However, in the DFT regime, either the results have not been very convincing or the explanation for the correspondence between the experimental and theoretical results has been missing. Particularly pertinent to the subsequent study is the development of method, which allows practical and reliable simulation of PES spectra including dynamical finite-temperature effects. The obtained results are compared with the experimental temperature-dependent PES of aluminum cluster anions (partially published in Ref. [76]).

The discussion in the previous section considered mainly the eigenenergy of the HOMO state alone. Since the high-resolution photoelectron spectroscopy gives in general a very detailed description of the electron levels in the probed system, it is now necessary to introduce into the treatment also the inner KS states, and their energy shifts v_{xc}^{∞} with respect to the true single-particle energies. At this point, it is worthwhile to remind that the following discussion does not consider any many-electron excitations i.e. a single-electron picture is retained. Furthermore, the photodetachment process is regarded as a vertical process, and the finite-lifetime effects of the consequent electron hole are neglected in the fashion of the original Koopmans' theorem.

In Figure 4.7, the energy shifts v_{xc}^{∞} for different (inner) electron shells are plotted as a function of eigenenergy. These results are obtained using the restricted (spherical) jellium model for 40 and 138 electron aluminum systems, and calculating the total energy differences between the neutral cluster and the ion, where the electron is removed from a single-particle level in question[4]. It is evident that v_{xc}^{∞} values for different orbitals are very close to each other: for 40 electron system the deviation is less than 0.2 eV, while for the 138 electron system it is only 0.1 eV. One can also see that the trend of v_{xc}^{∞} for both of these systems is slightly increasing for the inner KS states. For clarity, also the quantum numbers of different orbitals are displayed in Figure 4.7. Clearly, the s-states tend to have locally larger v_{xc}^{∞}, and that the v_{xc}^{∞} value decreases when the angular momentum l increases.

In the case of aluminum clusters, Fig. 4.7 gives the theoretical justification

[4]In many cases this approach is referred to as the ΔSCF scheme [7, 75].

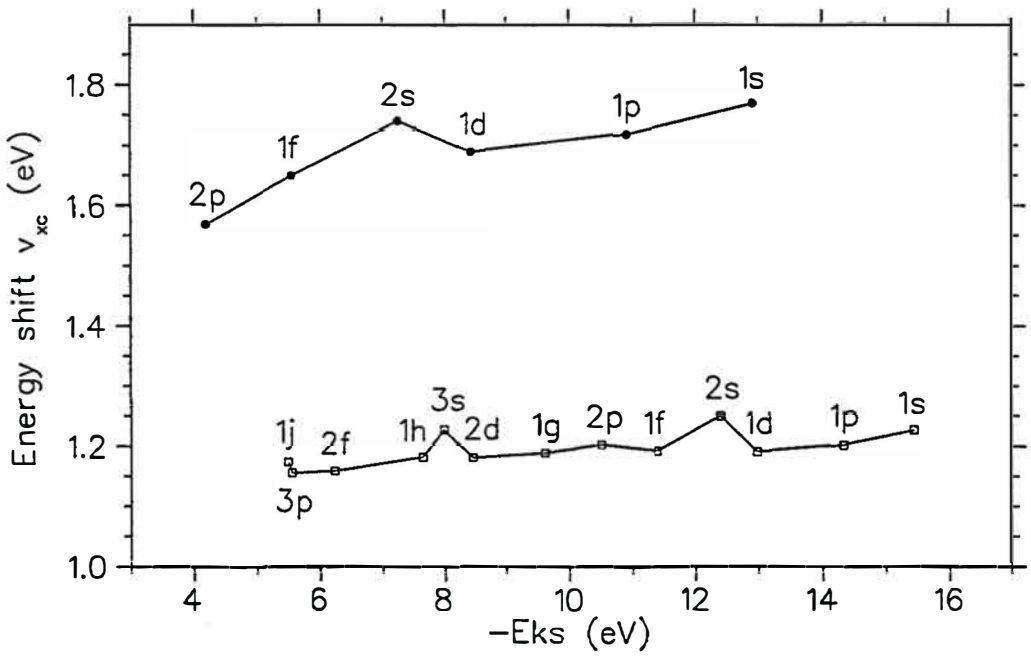

Figure 4.7: The energy shift v_{xc}^{∞} for different electron shells calculated using spherical jellium model. The upper and lower curves correspond to the 40 and 138 valence electron aluminum systems, respectively.

for the use of the energy shift v_{xc}^{∞} determined for the HOMO state also for the inner KS states. This approximation is especially successful near the Fermi energy. Consequently, a direct comparison with the experimental and theoretical PES for the corresponding cluster size can now be made, because it is possible to determine also the innercore detachment energies for the cluster anion isomers.

In practice, the method proceeds by plotting the density of the KS single-particle states (DOS), which is smoothed with a Gaussian and shifted by the mean value of v_{xc}^{∞}, and the low-temperature high-resolution PES in the same figure. It is well-known [72, 73, 74, 75] that the locations of the peaks, which correspond to the single-particle detachment energies, should coincide for the correct isomer. The relative intensity of these peaks can however vary, since (as before) the model does not take into account the different E1 cross sections of single-particle states. The finite width of the peaks of the PES is mainly due to the finite temperature, which makes the single electron eigenvalues to fluctuate due to the coupling to ionic motion. At low temperatures a harmonic approximation is adequate and leads to a Gaussian distribution of the single-particle levels. At elevated temperatures the cluster can visit

several isomers and the harmonic approximation is not valid. Consequently, at high temperatures the PES are determined using MD and time-averaged DOS.

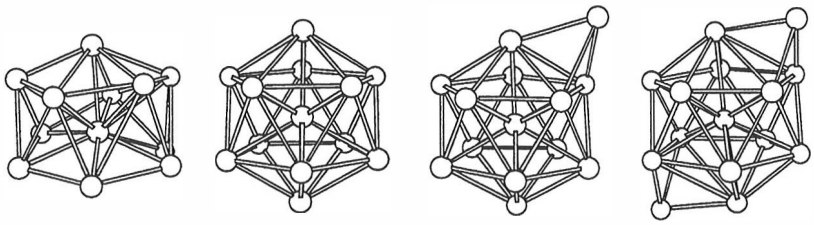

Figure 4.8: The ground state geometries of Al_{12}^--Al_{15}^- (left to right).

The ground state structures of Al_{12}^-–Al_{15}^- determined through structural optimization starting from those of the corresponding neutral ones (Sec. 4.1), are displayed in Fig. 4.8. In this size range, aluminum clusters prefer icosahedral packing: Al_{12}^- having an oblate deformed shape, Al_{13}^- being close to an ideal ICS, and Al_{14}^- and Al_{15}^- being capped icosahedra. For Al_{15}^-, it is found that the two capping atoms are located on the opposite sides of the "core" ICS, resulting a strongly prolate shape. The pattern of shape deformations for all the cluster anions shown in Fig. 4.8 correlates well with that obtained via jellium calculations for clusters with the number of electrons corresponding to the same size range (37 to 46 electrons) [77].

The measured PES spectra for Al_{12}^-–Al_{15}^- are shown in Figures 4.9 and 4.10 (solid line) in conjunction with the simulated temperature-dependent PES (dashed line). It is found that clusters leaving the nozzle early (short residence time) are quite "hot" whereas clusters leaving the nozzle late (long residence time) are "colder". Indeed the PES spectra for the cold clusters shown in Fig. 4.9 and the bottom panel of Fig. 4.10 exhibit well-defined features. On the other hand, hot clusters exhibit much broader and diffused spectral features, as shown in Figure 4.10 for Al_{13}^-, where spectra measured for three different residence times (labeled as "cold", "warm", and "hot") is displayed. Comparisons between the locations (binding energies) of the peaks and shoulders in the measured and simulated spectra for the cold clusters validate the v_{xc}^{∞}–shifting procedure of the calculated DOS described above. Especially visible is the consistency between the theoretical vertical detachment energy (vDE) values and the first maximum (HOMO state) in

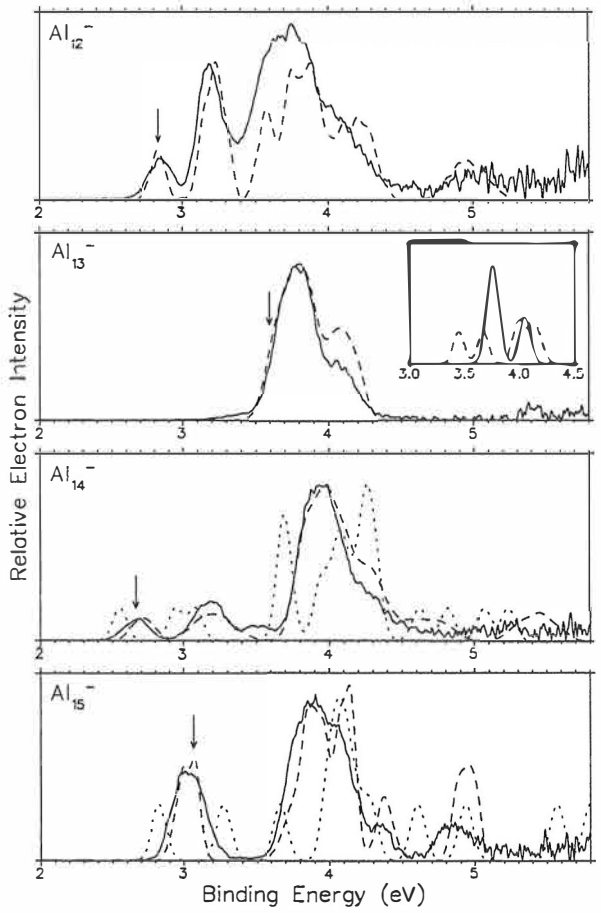

Figure 4.9: Measured photoelectron spectra of cold (long residence time) Al_{12}^-- Al_{15}^- at 193 nm (solid lines) compared to the simulated spectra (dashed lines). The simulation temperatures are 160, 260, 200, and 130 K for Al_{12}^-–Al_{15}^-, respectively. The arrows correspond to the vDE of the ground state structure at 0 K. The inset shows the Gaussian smoothed 0 K PES spectra for the ground state (solid line) and the decahedral isomer (dashed line) of Al_{13}^-. The dotted line for Al_{14}^- is the 0 K spectrum of the decahedral isomer, and that for Al_{15}^- the 0 K spectrum of an icosahedral-based isomer (see text).

the experimental PES for Al_{12}^-, Al_{14}^-, and Al_{15}^-. This suggests that the BO-LSD-MD method does not contain any systematic error in the vDE values of Al cluster anions. The widths of the peaks in the theoretical PES spectra originate solely from atomic thermal vibrations since at these low temperatures isomerization effects and/or strong shape fluctuations do not occur. The good agreement achieved here, without any adjustable parameters other than the ionic temperature in the MD simulations, strongly indicates that

the temperature of the "cold" clusters in the experiments is indeed well below the room temperature.

Theoretical PES spectra corresponding to isomeric structures of Al_{13}^-–Al_{15}^-, calculated at 0 K, are also shown in Fig. 4.9 (see inset for the threshold regions of Al_{13}^-, and the dotted line in the panels for Al_{14}^- and Al_{15}^-). The isomers for Al_{13}^- and Al_{14}^- are based on the 13-atom truncated decahedron (Fig. 4.1), and in the Al_{15}^- isomer two neighboring triangular facets of a 13-atom ICS are capped. Comparison between these spectra and those calculated for the ground state clusters as well as with the measured ones, suggests overall that at low temperatures either these isomers do not occur, or that their abundance in the cluster beam is rather low. In this context it is mentioned that starting from the decahedral isomer of Al_{13}^-, it transformed readily during short MD simulations into the ICS at about room temperature. This supports the conclusion pertaining to the low abundance in the cold beam of clusters "trapped" in isomeric structures; however, an even small relative (quenched) concentration of such isomer in the cold Al_{13}^- beam may be sufficient to account for the low-binding energy tail observed in the measured PES spectra for Al_{13}^- (see inset in Fig. 4.9).

Both the experimental and theoretical PES spectra, shown in Figure 4.10 for Al_{13}^-, which were measured at the three temperature regimes mentioned above and simulated at the indicated temperatures, exhibit gradual broadening and "smearing" of the PES spectral features as the temperature increases. It is also observed that the binding energy of the main peak is rather insensitive to the thermal conditions, while the line-shape near the threshold region (lower binding energies) exhibits a rather pronounced temperature dependence.

The broadening of the spectral features and the so called "thermal tail effect" near threshold originate from the variations of the electronic structure caused by enhanced vibrational motions at the higher temperatures, as well as from increased isomerization rates (e.g. in the "warm" regime) governed by the free-energy of the cluster (that is enhanced contributions of lower frequency modes to the vibrational entropy [78]), and from disordering ("melting") of the cluster in the "hot" regime, where inspection of the atomic trajectories reveals frequent transitions between a broad assortment of configurations. Indeed, examination of the vibrational DOS of the simulated clusters obtained via Fourier transformation of the atomic velocity autocorrelation functions revealed a marked gradual softening of the clusters at the "warm" and "hot"

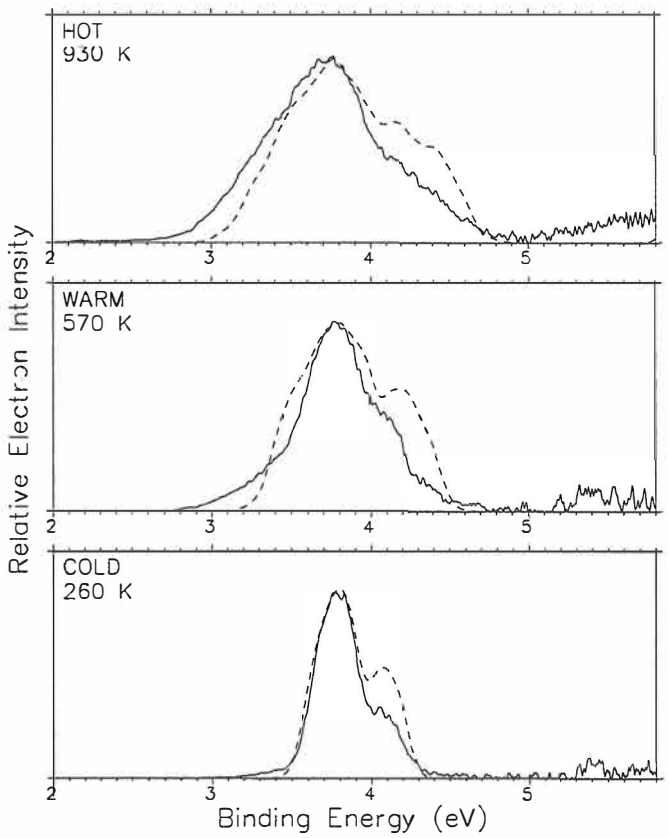

Figure 4.10: Measured temperature-dependent PES spectra of Al_{13}^- (solid lines) compared to the simulated ones at 930 K, 570 K and 260 K (dashed lines). HOT - short residence time, WARM - medium residence time, COLD - long residence time.

regimes (that is shifting of the vibrational spectrum to lower frequencies) coupled with increasing overlap between the frequency regions of the various modes due to large anharmonicities.

As a conclusion about Figures 4.9 and 4.10, it can be said that the overall agreement between the simulated and measured spectra and their thermal evolution is rather satisfactory, and the remaining discrepancies (mainly in line-shapes) may be attributed to insufficient sampling during the 5 ps MD simulations of the thermally-expanded phase-space of the clusters.

4.4 Larger aluminum cluster anions

The methodology developed in the previous section for practical calculations of finite-temperature PES spectra, through BO-LSD-MD simulations of aluminum cluster anions with no other adjustable parameters than the temperature, was demonstrated to yield results in agreement with high-resolution PES spectra measured at various thermal conditions of the cluster beam. Such comparative analysis allows reliable structural assignments and theoretical estimation of the clusters' temperatures. In this section, the developed structure determination method is further applied to larger aluminum cluster anions ($19 \leq N \leq 102$). Again, the optimal cluster geometries and the corresponding energies are determined using a steepest-descent-like minimization without any symmetry constraints. Most of the initial structures for this minimization were generated using a classical EMT ("effective medium theory") potential [65]. Some structures however had to be constructed "by hand" since EMT has some inadequacies as a geometry generator (e.g. 55-atom cubo-octahedron is not a stable local minimum). In order to make the study more comprehensive also ab initio molecular dynamics (time step of 3 fs) were used, in conjunction with simulated annealing. By optimizing configurations corresponding to local potential energy minima observed during such ab initio MD simulations it was possible to obtain additional low-energy isomers. Furthermore, lattice-based FCC-isomers, which had a maximal coordination number, were generated for larger cluster sizes ($N \geq 36$) using Monte Carlo (MC) simulations and a Metropolis algorithm.

Al_{19}^- isomers and their calculated PES (0 K) are presented in Figure 4.11 together with the experimental low-temperature high-resolution PES. The different isomers are presented in energetical order i.e. the lowest energy isomer 19(1) is the lowest. The geometrical structure of these clusters is easily seen. Isomer 19(1) is an oblate structure, where the internal structure of the cluster is mainly icosahedral. However the top of the cluster exposes a four-atom (100) facet, reminiscent of the truncated decahedron. The higher energy isomers 19(2) and 19(3) are also oblate and their internal structure is decahedral. Indeed, these isomers can be obtained by removing atoms from a 23-atom decahedron (see Fig. 4.1). Isomer 19(4) is a prolate double icosahedron. According to the EMT potential this is the ground state due to its high coordination number. Isomer 19(5) is a distorted octahedron, and it resembles the bulk Al most because of its FCC-like internal structure.

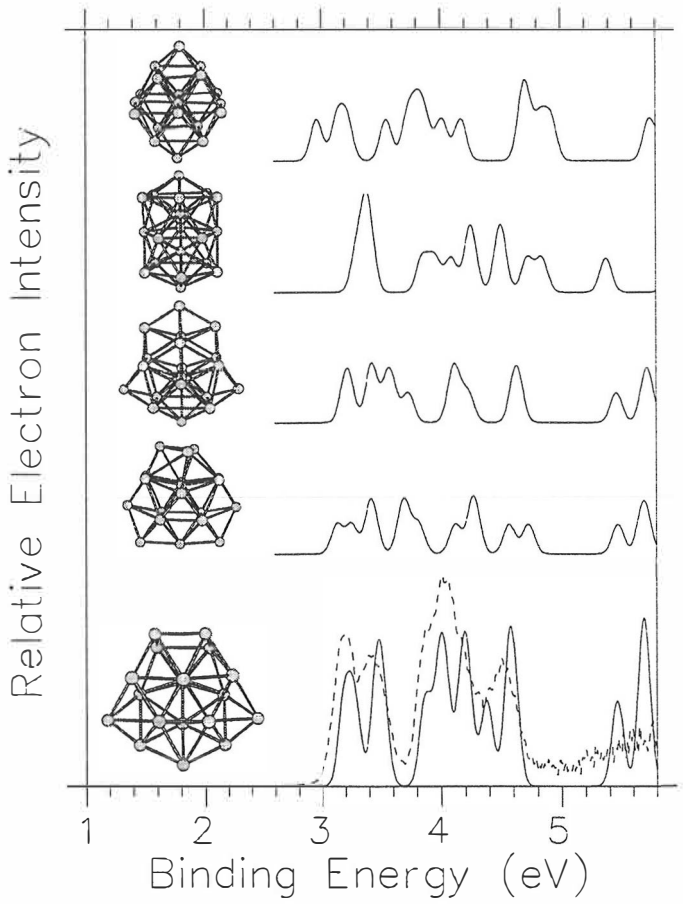

Figure 4.11: Al_{19}^- isomers in energetical order and their simulated PES (0 K) compared to the experimental high-resolution PES (dashed line) measured by 193 nm laser at cold temperature regime. The theoretical PES is obtained by smoothing the DOS by 0.13 eV FWHM Gaussians and replacing the resulting distribution by the calculated $v_{xc}^{\infty} = 1.47$ eV. The scaling of intensity between the theoretical and experimental PES is arbitrary.

It is evident that the theoretical PES of 19(1) in Fig. 4.11 is in a good agreement with the experimental PES. The locations of the peaks are consistent and also the two gaps in the experimental PES are reproduced. A direct comparison with the PES of other clusters shows clear differences, which also suggests that the experimental PES consists of only one specific isomer contribution. The high sensitivity of PES to the cluster geometry is apparent, since even the 19(2) and 19(3) isomers have considerably different spectra,

although their overall shape and internal structure are quite similar.

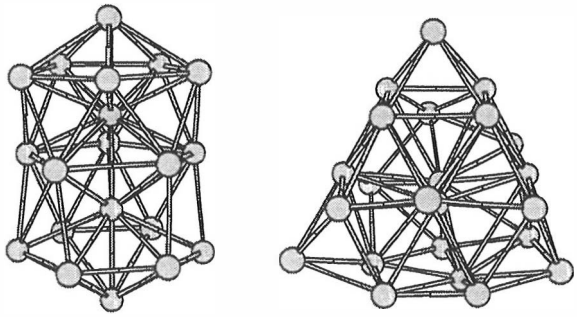

Figure 4.12: The ground state geometries of Al_{20}^- and Al_{23}^-.

The obtained ground state geometries of Al_{20}^- and Al_{23}^- are presented in Figure 4.12. Al_{20}^- is a prolate geometry and its internal structure is a hybrid of icosahedral stacking and hexagonal lattice. This is easily visualized by identifying a 13-atom ICS in the upper side of the cluster on top of a hexagonal ring, where the central atom has been pushed downwards. Al_{23}^- is an octupole deformed geometry with no specific internal structure. The cluster however resembles an octahedron (or pyramid) and FCC-stacking because of its two close-packed facets.

As for Al_{19}^-, also here the energetically lowest lying isomers of Al_{20}^- and Al_{23}^- give the best PES with respect to the experiments. For both of these isomers the specific features of the experimental PES are in a very good agreement. It is interesting to relate these features to the shell closings given by the jellium model. Al_{20}^- (61 valence electrons) shows a clear shell opening after Al_{19}^- (58 valence electrons) consistent to the spherical jellium model, which predicts that 58 is a magic number (i.e. shell closing). However, it should be emphasized here that these clusters are far from spherical. On the contrary, the PES of Al_{23}^- (70 valence electrons) does not fit into the spherical jellium results (shell closing after 68 electrons). Nevertheless, if the jellium model is modified to include also the self-deformations of electron density, it is observed that a system of 70 electrons prefers an octupole deformed shape [79, 80], which is consistent with the geometry of Al_{23}^-. The resulting DOS has a magic nature and a very large HOMO-LUMO gap, $E_g = 1.07$ eV.

Two Al_{36}^- low energy isomers and their theoretical PES compared to the

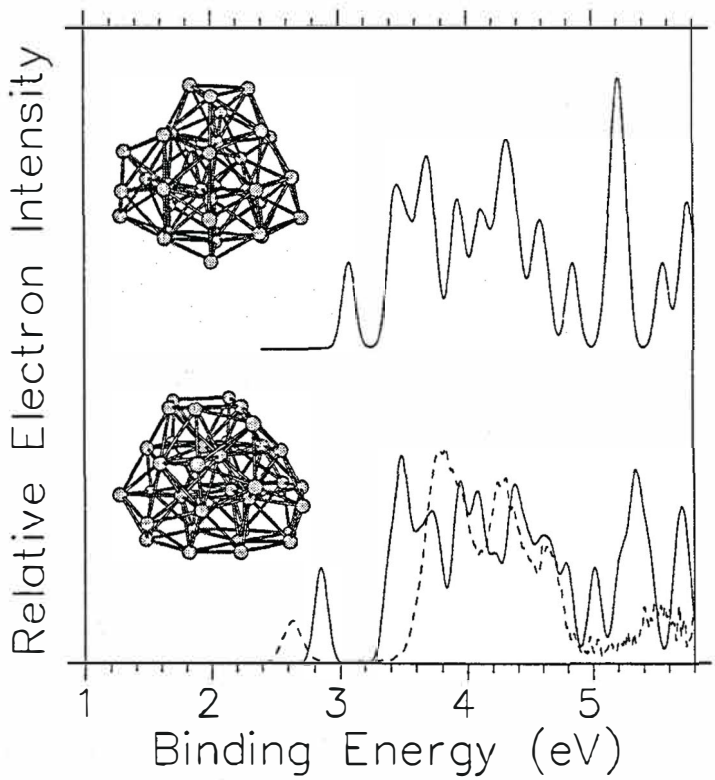

Figure 4.13: Two lowest energy isomers of Al_{36}^- in energetically reversed order and their simulated PES (0 K) compared to the experimental high-resolution PES (dashed line) measured by 193 nm laser at cold temperature regime. The theoretical PES is obtained by smoothing the DOS by 0.13 eV FWHM Gaussians and replacing the resulting distribution by the calculated $v_{xc}^{\infty} =$ 1.23 eV. The scaling of intensity between the theoretical and experimental PES is arbitrary.

experiments are presented in Figure 4.13. As opposite to the former Figure 4.11, the energetical order of the isomers in Fig. 4.13 is reversed i.e. isomer 36(1) is above isomer 36(2). This is done since isomer 36(2) has a better PES according to the experiments[5]. Evidently, isomers 36(1) and 36(2) do not have any specific internal structure. Also their overall shapes are not definite although one can see from the eigenvalues of the inertia tensor that these isomers are in fact very compact geometries (i.e. the shapes of the clusters are nearly spherical). It also seems that the clusters of this size

[5]The energy difference between these two isomers is only 15 K.

range start to produce facets. This can be seen most conveniently for the bottom of isomer 36(2), where a distorted (111) facet can be identified.

As seen from Figure 4.13, the experimental PES is not reproduced as satisfactorily as before. The most probable reason for this is that the correct ground state isomer is still not found. This is not surprising since the number of different isomers in this size range is enormous and the distorted internal structure of the low energy isomers even complicate the task. However, the opening of a new shell is seen in the theoretical PES after 108 electrons (Al_{36}^- has 109 electrons) for most of the low energy isomers. Especially for isomer 36(2), a very large 0.5 eV energy gap is seen between the HOMO-state and the underlying states, which is very considerable for this number of valence electrons. Nevertheless, the experimental gap is still almost twice as large.

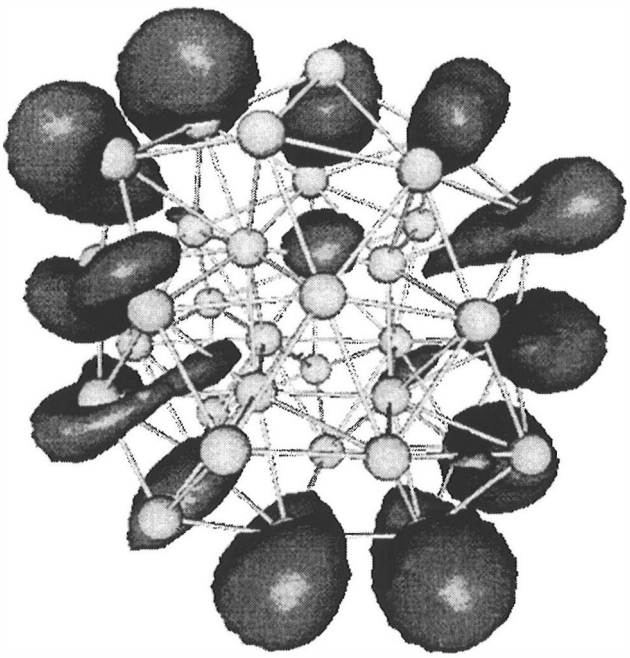

Figure 4.14: The charge density isosurface of the HOMO-state of the low energy isomer 36(2). The density value on the surface is -0.00036 a.u. and the charge accumulated inside the surface is -0.57 e.

In Figure 4.14 the charge density isosurface of the HOMO-state of isomer 36(2) is plotted. The cluster itself is seen from a top view with respect to the Fig. 4.13. The density value of the contour is 9% of the maximum density and the charge accumulated inside the contour is 57% of the total charge

of the single-particle state. Clearly, the charge has now delocalized at the surface of the cluster into the 12 nodes seen in Fig. 4.14. In addition, one should note that these nodes are more or less in plane. A spherical harmonics analysis according to equations (4.2) and (4.3), where the origin is in the center of charge and l goes up to 5 (atomic h-state), succeeds to cover only 18% of the corresponding KS single-particle density. This manifests that the HOMO-state in Fig. 4.14 contains remarkable contributions of higher angular momentum components ($l \geq 6$). It would be especially interesting to analyze the weight of $l = 6$ component since it is consistent with the 12 nodes in the density. Comparison to the underlying states shows that these states have a clearly different nature, and they are strongly delocalized throughout the whole cluster (i.e. the charge density also inside the cluster is considerable). This difference in orbital character correlates with the large energy gap between the HOMO-state and the underlying states in the theoretical PES.

Comprehensive studies of different isomers were also made for Al_{38}^- and Al_{55}^-. The lowest energy isomers of Al_{38}^- show similar distorted internal structures as Al_{36}^- isomers. However, in most cases it was possible to identify both decahedral and FCC-patterns in the cluster geometries. It became also evident that Al_{38}^- isomers tend to favor prolate overall shape deformations. This can be seen even in the 38-atom truncated octahedron (not a low energy isomer), which elongates according to one of its symmetry axis during optimization. On the contrary to the previous cluster sizes, the lowest Al_{55}^- isomers are MC-generated FCC-isomers, which have large close-packed (111) facets. According to this thesis, this is the first time in the larger cluster regime when the pure (optimized) FCC-clusters are energetically the most favourable structures. It was also noticed that the perfect 55-atom ICS and COS are unstable structures, which deform considerably during optimization resulting still poor total energies. Especially in the context of COS, it should be addressed that the six (100) facets are energetically unfavourable.

The theoretical PES of the low energy isomers of Al_{38}^- and Al_{55}^- show a certain correspondence with the experimental ones. The thresholds and the new shell opening of Al_{38}^- are in correct locations. Furthermore, the overall behaviour of Al_{55}^- is relatively nice. Conclusively, it can be however said that also for these cluster sizes (as for Al_{36}^-) the corresponding ground states are probably not found, which for these numbers of constituent ions is not surprising.

Furthermore, MC-generated FCC-isomers are calculated for Al_{52}^-, Al_{54}^-, Al_{79}^- and Al_{102}^-. All of these clusters contain large (111) facets due to the maximization of the coordination number. The resulting theoretical PES (except for Al_{102}^-) reproduce many of the experimental features quite well, but any conclusions about the ground states cannot be made since there is no comparison to other possible isomers. One should note here that even though an FCC-symmetry constraint would be used the number of well-coordinated different isomers is large in this size regime.

Table 4.2: Physical properties of larger aluminum clusters and cluster anions ($N \geq 36$): Cohesive energies per atom, HOMO-LUMO gap, vertical detachment energy, vertical ionization potential, and the mean nearest neighbour distance. Also the corresponding bulk aluminum values are displayed.

Cluster	E_C (eV)	E_g (eV)	vDE (eV)	vIP (eV)	$< d >$ (Å)
Al_{36}^-	3.13	0.40	3.07	5.81	2.77
Al_{38}^-	3.14	0.34	3.18	5.69	2.79
Al_{52}^-	3.20	0.12	3.20	5.67	2.81
Al_{54}^-	3.21	0.15	3.08	5.42	2.82
Al_{55}^-	3.21	0.23	3.24	5.28	2.83
Al_{79}^-	3.26	0.05	3.24	5.14	2.84
Al_{102}^-	3.31	0.09	3.44	5.18	2.84
Bulk Al	3.39[a]	0.00	4.25[b]	4.25[b]	2.86[b]

[a] From Ref. [81]
[b] From Ref. [26]

In Table 4.2 the physical properties of larger Al clusters and cluster anions are displayed in comparison with the bulk aluminum. The values for Al_{36}^-, Al_{38}^- and Al_{55}^- are achieved from the lowest energy isomers in the corresponding cluster size, and the other cluster sizes correspond to the aforementioned FCC-structures. As discussed previously, the cohesive energy E_C approaches asymptotically some theoretical estimate for the bulk value, which in LSD approximation is considerably exaggerated (3.70 eV, see Fig. 1.1). The HOMO-LUMO gap E_g seems to close up leading to the metallic nature of bulk aluminum. However, one must still consider also the symmetry and finite-size effects caused by the cluster geometry and electronic shell structure, which are seen in Tab. 4.2 as oscillations of E_g. The vIP and vDE values show a clear evolution towards the bulk work function W. In addition, their

size-evolutional trend (see Eq. (4.1)) seems to be quite similar since the mean value of these two quantities is close to W for all the cluster sizes. Comparison with the experimental IP and DE values [15, 76, 82] shows a good correspondence, although some deviations, which are mainly related to the IP determination method and different isomers, are observed. Finally, the mean nearest neighbour distance $< d >$ approaches the bulk value both asymptotically and monotonically. Interestingly, the $< d >$ value of Al_{102}^{-} is only 0.02 Å smaller than in the bulk, although the cluster mainly consists of surface atoms.

Chapter 5

Summary

In this thesis, small and medium-sized ($N \leq 102$) aluminum and sodium clusters are theoretically studied using the first-principles BO-LSD-MD simulation method [13], which exploits a DFT based KS formalism in conjunction with the LSD parametrization, separable nonlocal pseudopotentials and a plane wave basis set. The dynamical finite-temperature simulations of the clusters are performed using the BO approximation and the classical Hellmann-Feynman theorem of electrostatics. Consequently, the method is noticed to produce an efficient and reliable description of metal clusters within the LSD and pseudopotential regime.

One of the main topics of this thesis is the ionization potential of metal clusters, and the problems related to its determination. It is shown, that in order to obtain a real correspondence with the experiments and theory one has to consider also the experimental conditions, where especially the temperature plays a major role. Also the concept adiabatic IP and its applicability is discussed. Although this commonly used quantity usually produces good IP values with respect to experiments, it seriously fails in some occasions (Al_7) due to the remarkable relaxation of cluster caused by the ionization process.

For small aluminum clusters, the calculated aIP values generally agree well with the data from threshold ionization measurements. The initial rise of IP as a function of cluster size is understood in terms of increasing hybridization

of cluster orbitals derived from atomic s and p orbitals. Al_6 and Al_{13} have a clear shell structure in the jellium picture. The strong oscillations in the experimental data in the region $12 \leq N \leq 23$ are suggested to result due to a competition and coexistence of different isomers. The slightly contradictory IP values of Al_6 and Al_7 are further analyzed using molecular dynamics and the GKT formalism. The obtained PIE thresholds coincide with the experimental IP values lifting off the observed discrepancy. Furthermore, also the temperature-dependent ionization potential of sodium clusters ($N \leq 55$) is studied in terms of GKT. Partly in a semiempirical fashion, the experimental PIE curves are reproduced in a good agreement with the experiments. The obtained IP values for sodium clusters are systematically too large, which is related to the LDA approximation and used pseudopotential. It should be addressed that the good IP results obtained for the aluminum clusters are in a sense fortunate, since the LSD and pseudopotential approximations succeed extremely well in this case.

The temperature-dependent PES of aluminum cluster anions ($12 \leq N \leq 15$) is studied theoretically using molecular dynamics and the extended GKT formalism, which at least for aluminum[1] offers a straightforward connection between the theoretical DOS and the experimental PES. The obtained PES are in a very good accordance with the experiments allowing even a crude estimate for the cluster temperatures in the cluster beam. Furthermore, since the PES is very sensitive to the geometrical structure of the cluster, a reliable structure determination method for Al clusters anions is achieved. According to these findings, also larger aluminum cluster anions ($19 \leq N \leq 102$) are studied. It is observed that the BO-LSD-MD ground states for Al_{19}^-, Al_{20}^-, and Al_{23}^- produce the features of the experimental PES extremely well. For larger cluster sizes the search for the ground state dramatically complicates due to the exceedingly large number of different isomers, and the experimental PES is reproduced only in a qualitative manner.

The growth mechanism of Al clusters shows a gradual change around $N = 20$ from the icosahedral isomers to the less strained decahedral and FCC-stacked isomers. Already in the other DFT studies [11, 12, 23], the FCC-structures have been predicted to be energetically favourable in relatively small cluster sizes. In this thesis, it is however noticed that also the decahedral and

[1]Binggeli and Chelikowsky [74] successfully applied a similar approach for silicon clusters. On the contrary, Massobrio *et al.* [75] revealed that the technique does not apply for copper clusters.

significantly distorted FCC-resembling isomers provide good total energies. Furthermore, it is demonstrated that energetically the COS is a poor choice for a 55-atom FCC-cluster because of its large (100) facets. Instead, one should consider octahedrally grown FCC-structures, where the cluster mainly consists of the close-packed (111) facets. These results indicate that the octahedral (epitaxially grown) FCC-structures gain a dominant role quite rapidly, as it is indirectly observed in the experiments for Al_N ($N \geq 200$) clusters [83, 84, 85].

Bibliography

[1] R.S. Berry and H. Haberland, *Clusters of Atoms and Molecules*, (Ed. by H. Haberland, Springer-Verlag, Berlin 1994), pp. 1-12.

[2] W.A. de Heer, Rev. Mod. Phys. **65**, 611 (1993).

[3] W.D. Knight, K. Clemenger, W.A. de Heer, W.A. Saunders, M.Y. Chou, and M.L. Cohen, Phys. Rev. Lett. **52**, 2141 (1984); *ibid.*, **53**, 510(E) (1984).

[4] W. Ekardt, Phys. Rev. Lett. **52**, 1925 (1984); Phys. Rev. B **29**, 1558 (1984); *ibid.*, **31**, 6360 (1985); *ibid.*, **32**, 1961 (1985).

[5] M. Brack, Rev. Mod. Phys. **65**, 676 (1993).

[6] V. Bonacic-Koutecky, P. Fantucci, and J. Koutecky, Chem. Rev. **91**, 1035 (1991).

[7] R.O. Jones and O. Gunnarsson, Rev. Mod. Phys. **61**, 689 (1989).

[8] W. Kohn, Rev. Mod. Phys. **71**, 1253 (1999).

[9] J.A. Pople, Rev. Mod. Phys. **71**, 1267 (1999).

[10] Ray, M.F. Jarrold, J.E. Bower, and J.S. Kraus, J. Chem. Phys. **91**, 2912 (1989).

[11] J.-Y. Yi, D.J. Oh, and J. Bernholc, Chem. Phys. Lett. **174**, 461 (1990); Phys. Rev. Lett. **67**, 1594 (1991).

[12] H.-P. Cheng, R.S. Berry, and R.L. Whetten, Phys. Rev. B **43**, 10647 (1991).

[13] R.N. Barnett and U. Landman, Phys. Rev. B **48**, 2081 (1993).

[14] D.M. Cox, D.J. Trevor, R.L. Whetten, and A. Kaldor, J. Phys. Chem. **92** 421 (1988).

[15] K.E. Schriver, J.L. Persson, E.C. Honea, and R.L. Whetten, Phys. Rev. Lett. **64**, 2539 (1990).

[16] D.M. Cox, D.J. Trevor, R.L. Whetten, E.A. Rohlfing and A. Kaldor, J. Chem. Phys. **84**, 4651 (1986).

[17] M.F. Jarrold, J.E. Bower, J.S. Kraus, J. Chem. Phys. **86**, 3876 (1987).

[18] J. Persson, *Ph.D. Thesis*, (University of California, 1991).

[19] M.L. Homer, J.L. Persson, E.C. Honea, and R. Whetten, Z. Phys. D **22**, 441 (1991).

[20] H. Basch, W.J. Stevens and M. Krauss, Chem. Phys. Lett. **109**, 212 (1984).

[21] T.H. Upton, J. Phys. Chem. **90**, 754 (1986); Phys. Rev. Lett **56**, 2168 (1986); J. Chem. Phys. **86**, 7054 (1987).

[22] R.O. Jones, Phys. Rev. Lett. **67**, 224 (1991); J. Chem. Phys **99**, 1194 (1993).

[23] S.H. Yang, D.A. Drabolt, J.B. Adams and A. Sachdev, Phys. Rev. B **47**, 1567 (1993).

[24] J.F. Janak, Phys. Rev. B **18**, 7165 (1978).

[25] A. Szabo and N. S. Ostlund, *Modern Quantum Chemistry*, (First edition, Revised, Dover Publications, New York 1996).

[26] N.W. Ashcroft and N.D. Mermin, *Solid State Physics*, (International Edition, Saunders College Publishing, New York 1976).

[27] M. Born and J.R. Oppenheimer, Ann. Phys. **84**, 457 (1927).

[28] M. Weissbluth, *Atoms and Molecules* (Student Edition, Academic Press, New York 1978).

[29] R.P. Feynman, Phys. Rev. **56**, 340 (1939).

[30] R.G. Parr and W. Yang, *Density-Functional Theory of Atoms and Molecules* (Oxford Sciense Publications, New York 1989).

[31] P. Hohenberg and W. Kohn, Phys. Rev. **136**, 3864 (1964).

[32] M. Levy, Proc. Natl. Acad. Sci. (USA) **76**, 6062 (1979).

[33] W. Kohn and L.J. Sham, Phys. Rev. A **140**, 1133 (1965).

[34] W. E. Pickett, Comput. Phys. Rep. **9**, 115 (1989).

[35] N.W. Ashcroft, Phys. Lett. **23**, 48 (1966).

[36] M. Manninen, Phys. Rev. B **34**, 6886 (1986).

[37] N. Troullier and J.L. Martins, Phys. Rev. B **43**, 1993 (1991).

[38] N. D. Lang and W. Kohn, Phys. Rev. B **1**, 4555 (1970); *ibid.*, **3**, 1215 (1971); *ibid.*, **7**, 3541 (1973).

[39] M. Y. Chou, A. Cleland, and M.L. Cohen, Solid State Commun. **52**, 645 (1984).

[40] O. Genzken and M. Brack, Phys. Rev. Lett. **67**, 3286 (1991).

[41] H. Häkkinen, J. Kolehmainen, M. Koskinen, P.O. Lipas, and M. Manninen, Phys. Rev. Lett. **78**, 1034 (1997).

[42] I. Hamamoto, B. Mottelson, H. Xie, and X.Z. Zhang, Z. Phys. D **21**, 163 (1991).

[43] S. Frauendorf and V.V. Pashkevich, Z. Phys. D **26**, S98 (1993).

[44] S.M. Reimann, M. Brack and K. Hansen, Z. Phys. D **28**, 235 (1993).

[45] S.M. Reimann, S. Frauendorf and M. Brack, Z. Phys. D **34**, 125 (1995).

[46] H.A. Jahn and E. Teller, Proc. R. Soc. London Ser. A **161**, 220 (1937).

[47] M. Koskinen and M. Manninen, Phys. Rev. B **54**, 14796 (1996).

[48] C. Yannouleas and U. Landman, Phys. Rev. B **51**, 1902 (1995); *ibid.*, Phys. Rev Lett. **78**, 1424 (1997).

[49] P. A. M. Dirac, Proc. Cambridge Phil. Soc. **26**, 376 (1930).

[50] U. von Barth and L. Hedin, I. J. Phys. C **5**, 1629 (1972).

[51] D.M. Ceperley and B.J. Alder, Phys. Rev. Lett. **45**, 566 (1980).

[52] S.H. Vosko, L. Wilk and M. Nusair, Can. J. Phys. **58**, 1200 (1980); J. Phys. **C15**, 2139 (1982).

[53] J.P. Perdew, Phys. Rev. B **33**, 8822 (1986).

[54] J.P. Perdew, J.A. Chevary, S.H. Vosko, K.A. Jackson, M.R. Pederson, D.J. Singh, and C. Fiolhais, Phys. Rev. B **46**, 6671 (1992); *ibid.*, **48**, 4978(E) (1993).

[55] A.D. Becke, J. Chem. Phys. **96**, 2155 (1992).

[56] J.P. Perdew, K. Burke, and M. Ernzerhof, Phys. Rev. Lett. **77**, 3865 (1996); *ibid.*, **78**, 1396(E) (1997).

[57] J.P. Perdew and K. Burke, Int. J. Quantum. Chem. **57** (1996).

[58] M. Ernzerhof and G.E. Scuseria, J. Chem. Phys. **110**, 5029 (1999).

[59] J.C. Slater, Adv. Quantum Chem. **6**, 1 (1972).

[60] D.J. Tozer and N.C. Handy, J. Chem. Phys. **108**, 2545 (1998); *ibid.*, **109**, 10180 (1998).

[61] J.P. Perdew, R.G. Parr, M. Levy, and J.L. Balduz, Jr., Phys. Rev. Lett. **49**, 1691 (1982).

[62] J.P. Perdew and M. Levy, Phys. Rev. Lett. **51**, 1884 (1983).

[63] L. Kleinman and D.M. Bylander, Phys. Rev. Lett. **48**, 1425 (1982).

[64] L.T. Wille and J. Vennik, J. Phys. A **18**, L419, L1113 (1985).

[65] K.W. Jacobsen, J.K. Nørskov, and M.J. Puska, Phys. Rev. B **35**, 7423 (1987).

[66] H. Häkkinen and M. Manninen, J. Phys.: Condens. Matter **1**, 9765 (1989).

[67] M. Dupuis and B. Liu, J. Chem. Phys. **68**, 2904 (1978).

[68] W.A. Saunders, K. Clemenger, W.A. de Heer, and W.D. Knight, Phys. Rev. B **32**, 1366 (1985).

[69] W.A. Saunders, *Ph.D. Thesis* (University of California, 1986).

[70] M. Kappes, M. Schär, U. Röthlisberger, C. Yeretzian, and E. Schumacher, Che m. Phys. Lett **143**, 251 (1988).

[71] H.G. Limberger and T.P. Martin, J. Chem. Phys. **90**, 2979 (1989).

[72] V. Bonacic-Koutecky, L. Cespiva, P. Fantucci, J. Pittner, and J. Koutecky, J. Chem. Phys. **93**, 3802 (1990).

[73] V. Bonacic-Koutecky, P. Fantucci, and J. Koutecky, J. Chem. Phys. **100**, 490 (1994).

[74] N. Binggeli and J. R. Chelikowsky, Phys. Rev. Lett. **75**, 493 (1995).

[75] C. Massobrio, A. Pasquarello, and R. Car, Phys. Rev. Lett. **75**, 2104 (1995); Phys. Rev. B **54**, 8913 (1996).

[76] X. Li, H. Wu, X.-B. Wang, and L.-S. Wang, Phys. Rev Lett. **81**, 1909 (1998).

[77] C. Yannouleas and U. Landman, *Large Clusters of Atoms and Molecules*, (Ed. by T.P. Martin , Kluwer, Dordrecht 1996), p. 131.

[78] T. P. Martin, Phys. Rep. **95**, 167 (1983).

[79] S.M. Reimann, M. Koskinen, H. Häkkinen, P.E. Lindelöf and M. Manninen, Phys. Rev. B **56**, 12147 (1997).

[80] A. Rytkönen, H. Häkkinen, and M. Manninen, Phys. Rev. Lett. **80**, 3940 (1998).

[81] C. Kittel, *Introduction to Solid State Physics*, (Seventh Edition, John Wiley & Sons, New York 1996).

[82] M. Pellarin, B. Baguenard, M. Broyer, J. Lermé, and J.L. Vialle, J. Chem. Phys. **98**, 944 (1993).

[83] T.P. Martin, U. Näher, and H. Schaber, Chem. Phys. Lett. **199**, 470 (1992).

[84] U. Näher, U. Zimmermann, and T.P. Martin, J. Chem. Phys. **99**, 2256 (1993).

[85] S. Valkealahti, U. Näher, and M. Manninen, Phys. Rev. B **51**, 11039 (1995).